NASA Contractor Report 3733

# A Model for Nocturnal Frost Formation on a Wing Section

*Aircraft Takeoff Performance Penalties*

Mark A. Dietenberger

25th Anniversary
1958-1983

NASA

NASA Contractor Report 3733

# A Model for Nocturnal Frost Formation on a Wing Section

## Aircraft Takeoff Performance Penalties

Mark A. Dietenberger
*University of Dayton Research Institute*
*Dayton, Ohio*

**NASA**
National Aeronautics
and Space Administration

**Scientific and Technical
Information Branch**

1983

# TABLE OF CONTENTS

# LIST OF TABLES

# LIST OF FIGURES

# LIST OF SYMBOLS

c    is the airfoil chord length (m)

$c_p$    is the specific heat of different materials (J/g)

g    is the gravitational acceleration parallel to the surface $(m/s^2)$

h    is the overall heat transfer coefficient $(w/m^2 \, ^\circ K)$

$h_H$    is the convective heat transfer coefficient $(w/m^2 \, ^\circ K)$

$h_M$    is the convective mass transfer $(g/m^2 s)$

k    is the thermal conductivity of different materials $(w/m \, ^\circ K)$

$k_a$    is the thermal conductivity of air $(w/m \, ^\circ K)$

$k_s$    is the aerodynamic roughness height (m)

q    is the heat flux $(w/m^2)$

$q_s$    is the frost surface interface heat flux $(w/m^2)$

s    is the surface distance from stagnation point (m)

t    is the time (s)

x    is the distance from the plate or airfoil surface (m)

$x_s$    is the frost thickness (m)

A    is the aluminum slab area $(m^2)$

B    is the frost porosity

Bi    is the Biot number

$B_i$    is the frost porosity

$C_D$ is the drag coefficient

$C_f$ is the local friction coefficient

$C_o$ is a fitting constant in Equation (A3.10)

$C_L$ is the lift coefficient

D is the diffusion coefficient as a function of air temperature and ambient pressure

$F_e$ is the view factor to earth

$Gr_H$ is the Grashof number defined by Equation (A2.4)

H is the length from the plate leading edge to the frost formation location (m)

$I_{dH}$ is the sun's diffused radiation flux (w/m$^2$)

$I_N$ is the normal intensity of the sun (w/m$^2$)

$J_{sun}$ is the heat flux from the sun (w/m$^2$)

K is the frost thermal conductivity (w/m°K)

$K_N$ is the relative cloud cover

L is the airfoil segment length (m)

Le is the Lewis number

$L_e$ is the latent heat of evaporation (2500 J/g)

$L_s$ Is the latent heat of sublimation (2834.2 J/g)

Nu is the Nusselt number

$Nu_x$ is the local Nusselt number

P is the relative coverage of frost from the trailing edge to the leading edge of the airfoil.

Pr   is the Prandtl number

$P_v$   is the water vapor pressure ($N/m^2$)

R   is the reflection coefficient of ice

Re   Is the Reynolds number

$Re_x$   is the local Reynolds number

S   is the wing area ($m^2$)

Sc   is the Schmidt number

Sh   is the Sherwood number

$St_x$   is the local Stanton number

T   is the frost interior temperature (°K) (aircraft thrust in Equation 51)

$T_a$   is the air temperature (°K)

$T_d$   is the dew-point temperature (°K)

$T_s$   is the frost surface temperature (°K)

$T_w$   is the plate airfoil wall temperature (°K)

$T_\infty$   is the blackbody ambient temperature (°K)

$U_e$   is the potential flow surface velocities (m/s)

$U_\infty$   is the free stream velocity (m/s)

V   is the aircraft's speed

W   is the typical wing thickness (m) (aircraft gross weight in Equation 50)

$\alpha$   is the solar absorptivity of different materials (angle of attack in aircraft's equations of motion)

$\alpha_i$ is the angular deviation of the airfoil panel from the sun's horizontal direction

$\beta$ is the solar elevation angle

$\varepsilon$ is the blackbody emissivity of a material

$\varepsilon_I$ is the blackbody emissivity of ice

$\eta$ is defined by Equation (A2.3)

$\nu$ is the kinematic viscosity ($m^2/s$)

$\gamma$ is the flight trajectory angle from horizontal

$\xi$ is the boundary layer thickness ratio between the thermal thickness and the momentum thickness

$\rho$ is the density of different materials ($g/m^3$)

$\rho_a$ is the air density ($g/m^3$)

$\rho_f$ is the frost density ($g/m^3$)

$\rho_I$ is the ice density (0.917g/cc)

$\sigma$ is the Stefan-Boltzmann constant ($5.67 \times 10^{-8} w/m^2 K^4$)

$\phi$ is the angular deviation of the plate or an airfoil segment from the vertical direction

$\phi_a$ is the ambient relative humidity ratio

$\omega_a$ is the ambient absolute humidity

$\omega_s$ is the saturated absolute humidity at the frost surface temperature

$\Phi$ is defined by Equation (A2.6)

# SECTION 1

## INTRODUCTION

In colder climates the overnight frost accumulation on aircraft is a common occurrence. Langston [1] defined hoar frost as a uniform white deposit of fine crystalline texture which usually occurs on exposed surfaces on a cold and cloudless night and which is thin enough to clearly distinguish surface features underneath such as paint lines, markings and lettering. Ljungstroem [2] used the term hoar frost in the same way. In this paper we refer to nocturnal frost in the same sense, as the frost formed due to overnight blackbody cooling of surfaces.

In some countries, including the USA, regulations do not permit takeoff when frost, snow or ice is adhering to transport aircraft. In other countries, dispatch is permitted if, in the judgment of the flight crew, the accumulation will not affect the safety of the flight. For most commercial transports, any ice and snow can be removed by deicing equipment. Likewise, the nocturnal frost accumulated on the aircraft must also be completely removed prior to flight. This is usually achieved using costly and time-consuming glycol sprays. According to Ljungstroem [2] the airlines could experience a substantial savings if it were sufficient to clean only a small part of the wings and control surfaces. Brumby [3] mentioned that frost appears to have been a contributing factor in at least two recent takeoff accidents of transport aircraft. Weeks [4] "concluded that some combination of takeoff weight reduction and increase in takeoff speed will be necessary in order to maintain the normal safety margins in the presence of hoar frost deposits." Frost also presents a problem to general aviation aircraft, which have no effective means of frost removal. Thus a safety hazard may be present if a normal takeoff is attempted with frosted wings.

According to Brumby [3], for full wing span upper surface roughness beginning at the leading edge and extending varying distances aft, the typical effects are a reduction in maximum lift, a reduction in the angle of attack at which stall occurs, and a rapid post-stall drag increase. The effects become more adverse as the size and chordwise extent of the roughness increase. They may also be accompanied by a reduction in lift at a given angle of attack and by an increase in the wing parasite drag. Controversy concerning performance degradation with frost or snow on the wings may have arisen from tests on military aircraft showing that frost appeared to cause no degradation in takeoff performance. The tests, according to Langston, were directed only at establishing if the particular aircraft would take off at the handbook speeds. No attempt was made to determine how much the stall margin had been reduced by the frost. Langston [1], in citing this conclusion, added the observations that the hoar frost layer was up to 6 or 7 mm thick in rare cases. Weeks [4] stated that a frost deposit on the aircraft was typically 0.25 mm thick and an extremely severe deposit was about 1 mm thick. One wonders if the rare frost observed by Langston is actually rime frost due to overnight drizzles, which may produce a thickness of 6 to 7 mm. Thus, Langston [1] recommended that the frost should continue to be cleared off until better knowledge was obtained about frost and its effects on takeoff performance. According to Langston[1], once the aircraft is airborne, the frost usually dissipates rapidly due to aerodynamic heating and a lower atmospheric humidity. He suggested research areas to clear up the confusion concerning the safety of takeoff with a frosted wing.

This paper addresses several research areas suggested by Langston. In the second and third sections of this paper, the nocturnal frost formation model is described for the prediction of frost density and thickness as a function of time and varying

atmospheric conditions. This model was adapted and modified from the basic frost formation model developed by Dietenberger [5]. Comparison with a set of nocturnal frost formation experiments on a slightly inclined plate performed by UDRI in the 1980-81 winter is discussed in the fourth section. In the fifth section, an empirical relationship is developed for the lift, drag, and angle of attack penalties that would occur on a frost-coated airfoil as a function of the chord Reynold's number, the average roughness height to chord ratio, and the percent of frost-coated wing section. The data for the curve fittings was taken from Ljungstroem [2], Brumby [3], and others. The approach taken here is also a generalization of Brumby's method for the lift penalties. To a certain degree the results obtained can be extended to other wing section types and Reynold's number. Also, in this section, takeoff modifications due to aircraft roughness are suggested. In the last section, overnight atmospheric profiles are forecasted from the meteorological measurements at 5 p.m. according to equations obtained from Bagdonas, et.al. [6]. The nocturnal frost formation model was then used for a wing section, utilizing the air temperature, wind speed, relative humidity, pressure and the cloud cover as forecasted to calculate the frost thickness distribution on the wing section as a func-tion of time to 6 a.m. By making several computer runs with dif-ferent initial atmospheric data at 5 p.m., a graph of the average frost thickness versus air temperature, relative humidity, and wind speed was derived. Also comparisons were made between frost formation on unpainted versus painted wing sections for different cloud cover conditions. The frost thickness distribution was then converted to lift, drag, and the angle of attack penalties at takeoff speed for a general aviation aircraft using the empirical formulas from the previous section.

Applications of the results are as follows: if no aerodyna-mic penalties are expected at 6 a.m. as forecasted from 5 p.m.,

then no Flight Plan changes are required for the next morning. If nocturnal frost with significant aerodynamic penalties are expected at 6 a.m., then the pilot can take preventive measures such as put the aircraft in the hangar, cover the wings with plastic sheets, wait for the sun to dissipate the frost, or cancel the flight. If the preventive measures are not taken, and the pilot sees that the wing is covered evenly spanwise with nocturnal frost in the morning, and wishes to continue the flight plan, then some modified takeoff procedures are necessary. These procedures could be either a reduction in gross weight or an increase in the takeoff speed provided, of course, there is sufficient runway length and the angle of climb is high enough for obstacle clearance. An alternative procedure could be the partial removal of frost from the leading edge to about 10 to 15 percent of the chord length. This may considerably reduce or eliminate aerodynamic penalties. Accidents occur when ordinary takeoff procedures are used with a deteriorated wing section. This results in an inadequate safety margin above stall speed. Lastly, it is to be noted that a takeoff in the morning with nocturnal frost thicknesses uneven across the wing span could also be very dangerous. This could produce an asymmetric lift penalty across the wind span resulting in a wing drop, or rolloff at stall.

# SECTION 2

## NOCTURNAL FROST FORMATION/DISSIPATION ON A WING SECTION

In the basic frost formation model by Dietenberger [5], designed for refrigeration type applications, the wall temperature was held constant as a function of time. On an aluminum plate or airfoil exposed to the sky, the plate temperature will change with time because nocturnal radiation cooling of the plate will produce a plate temperature that is colder than that of the surrounding air. Therefore, the plate or wall temperature must be calculated as a function of time to determine when it reaches the frost-point temperature (Dietenberger [5]) and initiates frost. Thus, a model extending the Basic Frost Formation Model for calculating the wing section surface temperature due to radiation cooling was developed. The input data into the basic frost formation model consists of wall temperature, air temperature, ambient relative humidity, and the heat and mass transfer coefficient as a function of time. The model then calculates the frost surface temperature, the frost weight, and the frost thickness as a function of time. To adapt this model to nocturnal cooling, a few changes were necessary. The following section discusses the Noctural Frost Formation Model.

After a frost layer has formed on the aircraft throughout the night, the possibility exists that, in the morning, the sun may appear prior to the aircraft takeoff. The sun's flux and the convective heating may be sufficient to either melt or sublimate the frost. In fact, several minutes of sun's irradiation may be enough to remove all evidences of frost. Another source of frost dissipation was observed by Langston [1] when a breeze came up during the night. Thus, frost dissipation has been incorporated into the Noctural Frost Formation Model.

## 2.1 MODELING OF THE WING SECTION SKIN TEMPERATURE, $T_{W_i}$

To arrive at a model for calculating the airfoil skin temperature, an order of magnitude analysis of heat transfer terms was made. This allowed simplification of the heat balance equations. There are three heat transfer mechanisms that must be considered: radiative cooling of the surface, convective transfer of the surface to the air, and thermal conductivity within the frost/aluminum/air substances. Two terms that were used in this analysis are the Biot number,

$$Bi \equiv h\, W/k_{skin} \qquad , \qquad (1)$$

and the heat content, $\rho c_p$, of different materials that would show a transient temperature property.

According to the Handbook of Heat Transfer [7], if $Bi \leq 0.1$ the temperature distribution within the plate or piece of the wing section skin, may be considered uniform with an error less than 5%. Consider first the wing section supporting structure. Assume it is made of aluminum with a thermal conductivity of $k_{skin}=202.4$ w/mC. Also assume the conservative estimate of the airfoil thickness is approximately W=0.5m. Taking Bi=0.1 as the critical value, we can estimate the value of h that would allow us to make simplifying assumptions, that is:

$$h_{crit} = \frac{0.1\ k_{skin}}{W} = 40.48 \quad W/m^2{}^{\circ}C \qquad (2)$$

The heat transfer coefficient, $h_H$, in forced convection is typically below 30 $W/m^2{}^{\circ}C$ for a wind speed of 5 m/s. Of course, the effective radiative heat transfer coefficient, $h_r$, introduces an additional term for comparison with $h_{crit}$. But $h_r$ is typically less than 5 $W/m^2{}^{\circ}C$ for surface emissivity of 1.0 and at freezing temperatures. The equivalent radiation thermal conductivity in the air pockets can be estimated by $k_r = \epsilon_{Al}\, h_r\, W$, or substituting in $\epsilon_{Al} \simeq 0.2$ and in the above values we get

6

$k_r = 0.5$ W/m$^2$°C as the upper limit. The air thermal conductivity, of about 0.025 W/m°C and $k_r$ can be ignored as they are much smaller than $k_{skin}$. Thus we need to be concerned about the conductive temperature gradient in the wing spar structures along thickness of the wing section only in an approximated fashion. Also the total mass of the spars is about one-half of the wing's mass.

If the wing aluminum skin thickness is typically about W = 0.3 cm, which gives $h_{crit}$=6747 W/m$^2$°C, then the temperature gradient across the thickness can be considered to be zero. On the other hand, if we take W=chord length of the airfoil of about 5m, then $h_{crit}$= 4.048 W/m$^2$°C. This is a typical natural convection value of $h_H$, which means a strong enough chord-wise distribution of the temperature gradient will exist on the wing section skin. Thus the study of the Biot number shows that the macroscopic dimensions of the airfoil will show perceptable degree of temperature distribution, but in the microscopic dimensions, such as that of aluminum slab, the skin temperature can be considered to be uniform.

If any material has a heat content, $\rho c_p$, and a thermal conductivity much lower than other materials, then it can be ignored in the analysis. For example, the air pocket within the wing section has a heat content, $\rho_a c_{p_a}$ = 0.001397 J/m$^3$°C, as compared to the heat content of the aluminum, $\rho_{Al} c_{p_{Al}}$ = 2.368J/m$^3$°C. Likewise, air has thermal conductivity of 0.25 W/m°C compared to $k_{Al}$ = 202.4 W/m°C. The smallness of the air thermal conductivity drastically reduces the bulk effect of the air pockets. Thus, the air pocket can be neglected as a heat sink without introducing serious errors in calculating the wall temperatures. On the other hand, the heat content of ice is $\rho_i c_{p_i}$ = 1.88 J/m$^3$°C and a thermal conductivity of about 2.5 W/m°C. It is noted that the heat content and thermal

conductivity of frost would be between that of air and ice, and if the frost density is sufficiently high, then the frost cannot be ignored as a heat sink without introducing errors in the wall temperatures. If, in addition, a fuel tank is located in some section of the wing and the tank is filled with kerosene, the heat content of the tank would be that of kerosene, $\rho_k C_{p_k} =$ 1.52 $J/m^3{}^\circ C$. Thus kerosene in this case could be an important heat sink/source if there is an efficient conduction path to the skin. It is noted, however, that the thermal conductivity of kerosene, $k_k = .1748$ w/m°C, is much lower than that of the aluminum, $k_{Al} = 202.4$ W/m°C. Thus, initially, kerosene would not be an important heat sink/source. It is noted if the tank is closely attached to, say, the leading edge of the airfoil, and is filled with kerosene, then it may be possible to retard frost formation overnight by preventing the wall temperature from reaching the frost-point temperature.

Based upon the order of magnitude analysis just provided, the formulation of the wall temperature, $T_{w_i}$, should be consistent with the following:

1) The spanwise and chordwise temperature distribution on the airfoil skin is a slowly changing function of time and position.

2) The ith aluminum slab area $A_i$ is at uniform temperature so that it can be treated as a lump system.

3) The aluminum slab, the spar supporting structures, and the frost layer are significant heat sources/sinks.

4) The effect of the fuel tank on the airfoil skin temperature distribution is considered minor due to typical locations and conduction path to the surface. Later, it is shown how this assumption can be relaxed.

5) Heat radiation exchanges within the airfoil are negligible at around freezing temperatures.

8

Since a lump system analysis is being pursued, several special cases of heat transfer balances on an aluminum slab are considered. The heat balances equations, for example, differ for a non-frosted and a frosted slab. If the dew point is above the frost point, condensation may occur and then freeze. This requires a modification in the heat balance equation. Also the attachment or the non-attachment of the supporting structures to the aluminum slab will result in different heat balances. Even for a frosted slab there are different heat balances between when the frost is forming and dissipating. It is our objective to treat all possible cases. The following discusses the heat balance equation used to obtain the aluminum skin temperature for each case. The skin temperature is then used as the wall temperature in the frost formation model.

Case A. Clean slab of an airfoil segment not connected to supporting structures is shown in Figure 1. Four energy terms are involved. They are the enthalpy rate, convective heat, radiative heat, and the conductive heat within the skin. Thus we obtain the heat flux equation in the difference form in order to solve for $T_{W_i}$ as a function of time:

$$\rho_{Al} c_{pAl} W_i \frac{dT_{w_i}}{dt} = h_{Hi}(T_a - T_{w_i}) + \sigma \varepsilon_{Al} [T_\infty^4(1-F_e) + (\varepsilon_e T_e^4 + (1-\varepsilon_e)T_\infty^4)Fe$$

$$-T_{w_i}^4] + \alpha_{Al} J_{sun} + k_{Al} W_i \left[ \frac{T_{w_f} - T_{w_i}}{L_i(L_f+L_i)/2} + \frac{T_{w_b} - T_{w_i}}{L_i(L_b+L_i)/2} \right] \qquad (3)$$

where:

$$J_{sun} = I_N(\cos\beta \cos\alpha_i \cos\phi_i + \sin\beta \sin\phi_i) + I_{dH}(0.42$$

$$+ \{[\cos\phi_i \cos^6 (\tfrac{\pi}{4} - \tfrac{\beta}{2})]^2 + [0.58 \sin\phi_i]^2\}^{1/2})$$

$$+ (1-\varepsilon_e)F_e(I_N \sin\beta + I_{dH}) \qquad (4)$$

$$F_e = 1/2(1-\sin\phi_i) \text{ for infinite earth surface area.} \qquad (5)$$

9
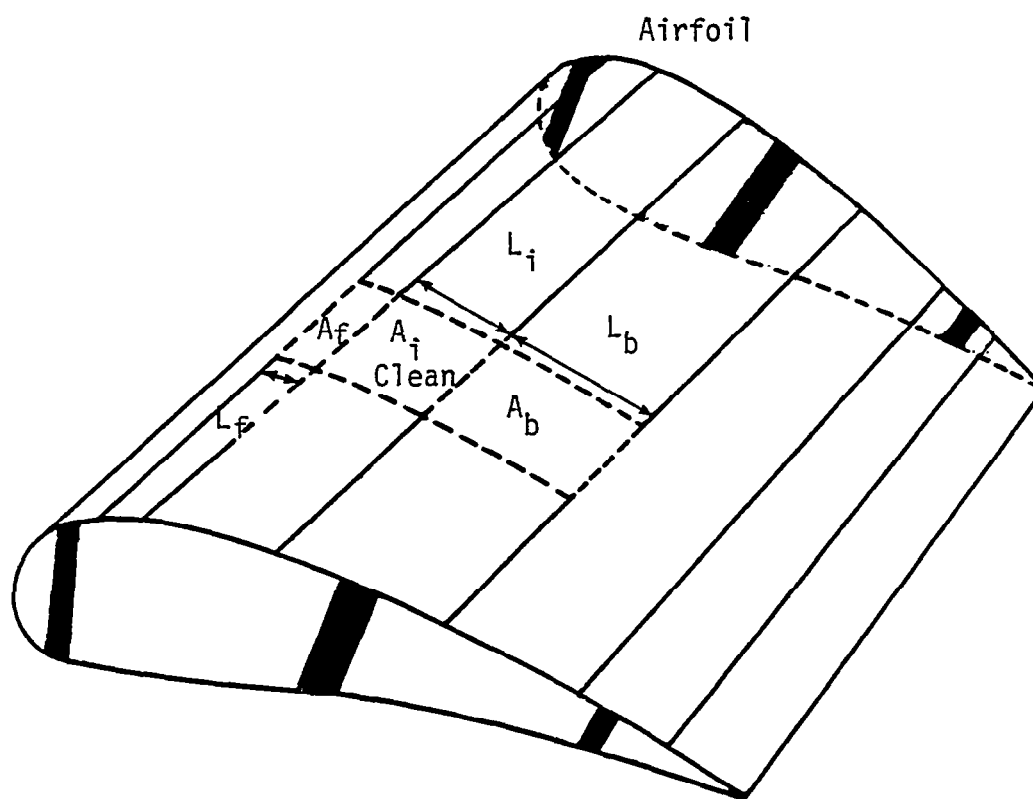
Figure 1. Non-frosted Slab Area, $A_i$, without a Spar Structure Underneath

$$T_\infty = T_a \left[1 - (0.5 - 0.006 \ \sqrt{\overline{P_v}})(1 - K_N)\right]^{1/4} \qquad (6)$$

$T_a$ = ambient temperature at a height of 1.5 meters

$$K_N = \begin{cases} 0.31 & 100\% & \text{cirrostratus} \\ 0.63 & 100\% & \text{altostratus} \\ 0.85 & 100\% & \text{stratus} \\ 0.99 & 100\% & \text{nimbostratus} \\ 0.0 & & \text{clear night} \end{cases} \qquad (7)$$

Equation (4) was developed from Thermal Environmental Engineering [8], and Equation (6) was obtained from Bagdonas, et.al. [6].

For the explanation of each symbol, the reader is referred to the List of Symbols. Some observations can be made of the heat flux equation. The first is that for a quiet, clear, over-night situation, where $J_{sun}$=0, and $h_H$ is small, the dominant heat flux term for cooling of the aluminum slab to occur must be the radiation term. The cooling of the slab is retarded if the air-foil surface has a very low long-wave emissivity, $\varepsilon_{Al_e}$. For polished aluminum, the $\varepsilon_{Al_e}$ typically has a value of 0.05. For unpolished and oxidized aluminum, $\varepsilon_{Al_e} \cong 0.2$. Since most paints have long-wave emissivities around 0.85, a significantly colder surface and earlier frost initiation would be expected on a painted airfoil. Thus to retard frost formation on an airfoil it is important to keep the airfoil cleaned and shined to maintain a low value of the long-wave emissivity. In the morning, when the sun shines on the airfoil, it is desirable to have maximum heating of the aluminum slab to melt or dissipate any frost. Therefore, the short-wave emissivity, $\varepsilon_{Al_{sun}}$, should have a high value to maximize the sun's heat flux to the airfoil. For a polished aluminum, $\varepsilon_{Al_{sun}}$ is typically at about 0.2, and for unpolished and oxidized aluminum, $\cong 0.5$. If possible, a special purpose paint could be utilized to obtain a high value of $\varepsilon_{Al_{sun}}$, but a low value of $\varepsilon_{Al_e}$.

11

In the general literature of numerical methods on a system of first order differential equations, there are usually two ways of solving Equation (3) for $T_{W_i}$. One way is to use a predictor-corrector integration scheme, and the other way is to use backward differencing or implicit schemes. From Shampine [9] we find that for a high transient or "non-stiff" problem, predictor-correctors are appropriate, and if the problem is slow changing or "stiff," then implicit schemes should be used. Experimentation with both type of schemes has shown that Equation (3) is definitely a "stiff" problem. By making the following approximations:

$$\frac{dT_{w_i}}{dt} \simeq (T_{w_i}^{t} - T_{w_i}^{t-\Delta t})/\Delta t \tag{8}$$

and:

$$(T_{w_i}^{t})^4 \simeq (T_{w_i}^{t-\Delta t})^3 (4T_{w_i}^{t} - 3T_{w_i}^{t-\Delta t}) \tag{9}$$

and substituting into Equation (3), we then obtain a linear system of equations which was solved by standard methods. It turns out that for a "stiff" system a proper choice of a backward differencing scheme will be stable no matter what the time increment is. Consequently, the time increments are limited by the accuracy desired in numerical integration. Thus, Shampine [9] and others offer a robust code to solve a system of first-order differential equations. However, Equation (3) becomes highly nonlinear when condensation, ice, and frost growth, and the calculation of heat and mass transfer coefficients are eventually included in the model. This requires Equation (3) to be iterated at a given time step, a feature not available in the robust codes examined. However, we note the present iteration scheme utilized is conditionally convergent, that is, only in rare cases do the panel temperatures fail to converge when the number of iterations is large.

Case B. An ith slab with spar supporting structures attached between the ith slab above and the jth slab below is shown in Figure 2. The contribution to Equation (3) for the solution of $T_{w_i}$ due to the spar support is included as follows.

In a manner analogous to conduction between adjoining slabs, a thermal conduction term was added to the right side of Equation (3) for conduction through the spar. This term is:

$$q_{spar} = \left( \frac{W_{spar}}{L_i} \right) \left( \frac{k_{Al}}{H_{spar}} \right) (T_{w_j} - T_{w_i}) \tag{10}$$

A heat capacitance factor was added to the left side of equation (3) as:

$$q_{spar\ capacitance} = \left( \frac{W_{spar}}{L_i} \right) \left( \frac{H_{spar}}{2} \right) \rho_{Al}\ c_{pAl}\ \frac{dT_{w_i}}{dt} \tag{11}$$

We note that the ratio $W_{spar}/L_i \leq 1$ acts as a normalization heat flux factor to account for the difference in the attached surface area versus the ith slab surface area. The other conduction terms in Equation (3) also show a normalization heat flux factor with respect to the adjoining slabs. Lastly, a kerosene tank could be incorporated in the same way as was done for the spar structure. The present model does not include this capability.

Case C. A water film exists on the ith slab when the wall temperature, $T_{w_i}$, is below the dew-point temperature, but at or above the freezing temperature. The water film is assumed to be very thin, thus not contributing any heat capacitance effects. On the other hand the latent heat flux must be included and is added to the right side of Equation (3) at the appropriate time in the iteration to converge on the $T_{w_i}$'s as:

$$q_{liquid\ latent} = L_e\ h_{M_i} (\omega_a - \omega_{s_i}) \tag{12}$$
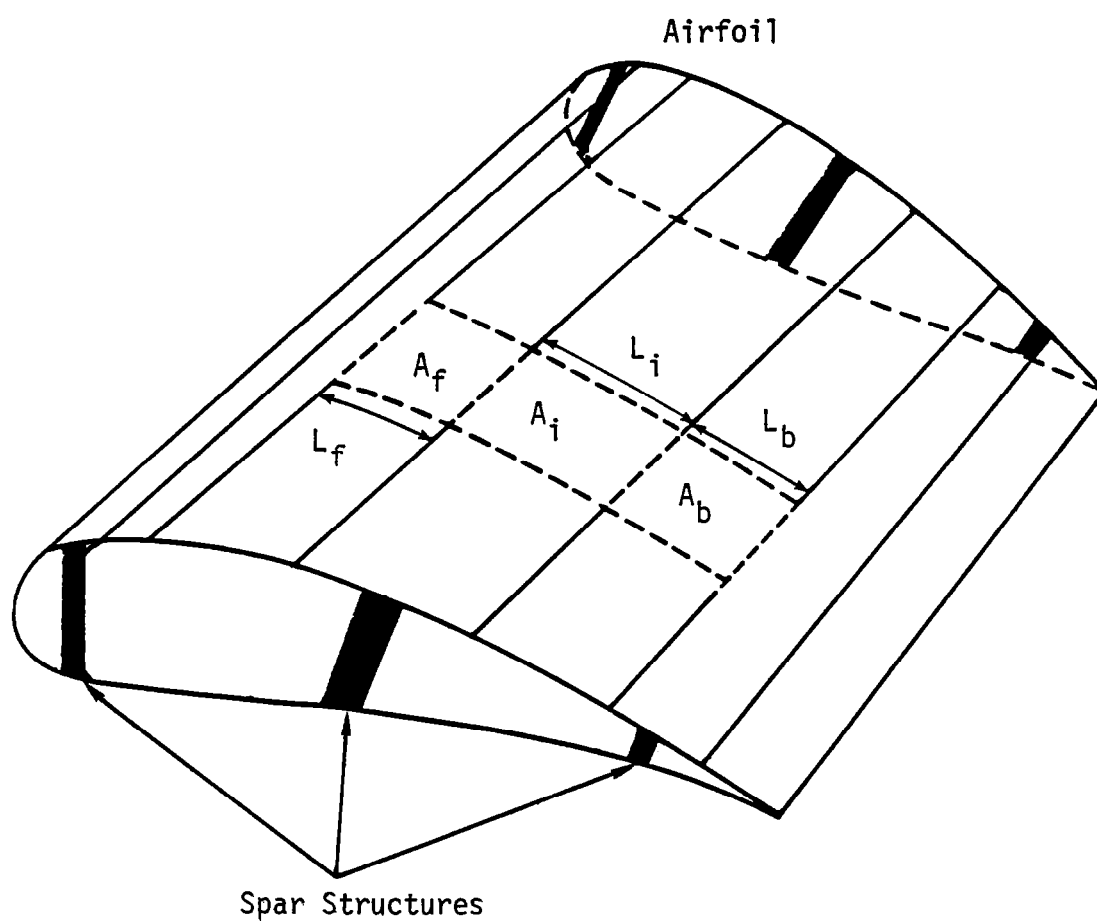
Figure 2. Non-frosted Slab Area, $A_i$, with a Spar Structure Underneath.

Case D. Frost or ice exists on the ith slab when the wall temeprature, $T_{w_i}$, is below the frost-point temperature and below the freezing temperature. If the frost-point temperature equation is calculated to be above the freezing temperature, then it is likely that ice will exist due to freezing of dew. If the frost-point temperature is below the freezing temperature, then frost growth is automatically predicted. The ice growth (or frost/ice melting) is calculated from the net heat flux at the ith slab when the ice/frost surface temperature is set at the freezing temperature. If the calculated ice growth flux exceeds the convective mass flux, then frost growth is predicted instead. The above conclusions concerning frost or ice growth is not finalized until Equation (3) has converged with respect to the wall temperature distribution, $T_{w_i}$, at a given time step. Since Equation (3) is being solved implicitly and iteratively, a feedback mechanism from the ice or frost growth is incorporated. Thus Equation (3) is further modified by the following heat flux contribution. The heat capacitance flux of the frost/ice is added to the left side of Equation (3) as:

$$q_{frost/ice\ capacitance} = \left[ \rho_I\ c_{pI}\ x_{I_i} + \rho_{f_i}(1-B_i)c_{pI}\ x_{s_i} \right] \frac{dT_{w_i}}{dt} \quad (13)$$

The conductive heat flux due to frost or ice is added to the right side of Equation (3) as:

$$q_{frost/ice\ conductance} = \frac{630}{T_{w_i}}(x_{I_i} + (1-B_i)x_{s_i}) \left[ \frac{T_{w_f} - T_{w_i}}{L_i(L_f+L_i)/2} \right.$$

$$\left. + \frac{T_{w_b} - T_{w_i}}{L_i(L_b+L_i)/2} \right] \quad (14)$$

The latent heat flux due to frost formation is added to the right side of Equation (3) in place of Equation (12) as:

$$q_{frost\ latent} = L_s\ h_{M_i}(\omega_a - \omega_{s_i}) \quad (15)$$

15

For the latent heat flux due to ice formation Equation (12) is retained.  A fusion heat flux is also added to the right side of Equation (3) as:

$$q_{ice\ fusion} = (L_s - L_e)\ \rho_I\ \frac{dx_{I_i}}{dt} \qquad (16)$$

Finally, changes in the wing section surface emissivities occur due to the presence of ice or frost.  The blackbody emissivity of the surface is modeled in Appendix I as:

$$\varepsilon_{surface} = B_i \left[ \varepsilon_{ice} + (\varepsilon_{Ale} - \varepsilon_{ice})\ e^{(-10^5\ x_{I_i})} \right] + (1 - B_i)$$
$$\times \left[ \varepsilon_{ice} + (\varepsilon_{Ale} - \varepsilon_{ice})\ e^{-10^5(x_{I_i} + x_{S_i})} \right] \qquad (17)$$

where $x_{I_i}$ and $x_{S_i}$ are ice and frost thickness, respectively, in meters, and $B_i$ is the frost porosity.  The above model of the surface is based on the assumption that the radiative absorption is dominant and the radiation scattering is minimized.  Thus when $x_{I_i}$ and $x_{S_i}$ get large, the surface emissivity approaches the emissivity of ice.  On the other hand, when $x_{I_i}$ and $x_{S_i}$ are very small, the surface emissivity approaches that of aluminum (providing the wing is unpainted).  The porosity $B_i$ weights emissivity according to blackbody radiation penetration of the frost layer.  Likewise, solar absorptivity is formulated as:

$$\alpha_{surface} = B_i \left[ \alpha_{ice} + (\alpha_{Al} - \alpha_{ice})\ e^{-10 x_{I_i}} \right] + (1 - B_i)$$
$$\times \left[ \alpha_{ice} + (\alpha_{Al} - \alpha_{ice})\ e^{-10(x_{I_i} + x_{S_i})} \right] \qquad (18)$$

This equation is based on the same assumption about radiation absorptions through the frost/ice.

Given the calculation of the heat and mass transfer coefficients and of the frost density and thickness, the solution of Equation (3), with all the additional terms up to Equation (18), can reliably compute the wing section surface temperature distribution.  With additional modifications, the full wing could

be modeled. However, the present model considers only a cross-section of the wing.

## 2.2  MODELING OF THE NOCTURNAL FROST ON ITH SLAB

In the earlier discussion on the heat content, it was shown that the heat content of ice is about the same as that of the aluminum. Thus the frost is expected to show some significant enthalpy heat rate at high frost densities. This situation results in a coupling for the energy equations of the frost and of the aluminum slab. The heat flux conducted horizontally from the other frosted slabs through the frost layer is considered quite minor as compared to the heat flux conducted horizontally through the aluminum slab because the thermal conductivity of ice, $k_{ice} \cong 3$ W/m°K, is much less than the aluminum thermal conductivity, $k_{Al}=202$ W/m°K. Thus the heat transfer equation for frost formation becomes one-dimensional:

$$\rho_{f_i} \, c_{pf} \, \frac{\partial T_i}{\partial t} = \frac{\partial}{\partial x} \left( K_i \, \frac{\partial T_i}{\partial x} \right) \tag{19}$$

with the frost thermal conductivity from Dietenberger [5]. Equation (19) is subjected to the boundary conditions:

$$q_{s_i} = K_{i} \frac{dT_i}{dx} \bigg|_{x=x_{s_i}} = h_{H_i}(T_a - T_{s_i}) + h_{M_i} L_s(\omega_a - \omega_{s_i}) + \alpha_{fr} J_s$$

$$+ \sigma \varepsilon_{fr_e} \left[ T_\infty^4 (1 - F_e) + \left( \varepsilon_e T_e^4 + (1 - \varepsilon_e) T_\infty^4 \right) F_e - T_{s_i}^4 \right], \tag{20}$$

$$\frac{\partial T_i}{\partial t} \bigg|_{x=0} = \frac{\partial T_{w_i}}{\partial t} \quad \text{and:} \tag{21}$$

$$\frac{\partial T_i}{\partial t} \bigg|_{x=x_{s_i}} = \frac{\partial T_{s_i}}{\partial t} \tag{22}$$

Since an analytical solution is not possible, a numerical and a polynomial function approach toward the problem is pursued.

Let $\frac{\partial T_i}{\partial t} = ax + b$, and apply the boundary conditions to get:

$$\frac{\partial T_i}{\partial t} = \left(\frac{\partial T_{s_i}}{\partial t} - \frac{\partial T_{w_i}}{\partial t}\right) \frac{x}{x_{s_i}} + \frac{\partial T_{w_i}}{\partial t} \qquad . \qquad (23)$$

Then the heat equation for the frost is integrated to get:

$$\int_{T_{w_i}}^{T_{s_i}} K(T)\, dT = \rho_f\, c_{p_f}\left(\frac{ax_{s_i}^3}{6} + \frac{bx_{s_i}^2}{2}\right) + cx_{s_i} \qquad (24)$$

$$q_i = c, \text{ and } q_{s_i} = \rho_f\, c_{p_f}\left(\frac{ax_{s_i}^2}{2} + bx_{s_i}\right) + c \qquad (25)$$

Combining the last two equations, substituting in values for a and b, and rearranging, the expression for $q_i$ is obtained as:

$$q_i = q_{s_i} - \rho_{f_i}\, c_{p_f}\, x_{s_i}\left(\frac{\partial T_{s_i}}{\partial t} + \frac{\partial T_{w_i}}{\partial t}\right)/2, \qquad (26)$$

which means the heat flux arriving at the slab through the frost structure is the heat flux from the ambient air minus the average frost enthalpy heat rate. Physically, this makes sense in that the frost layer can be treated almost as a lump system.

To calculate the frost surface temperature, $T_{s_i}$, the constants a, b, and c from the integration of the heat equation for the frost are replaced by their equivalents. The result is:

$$\int_{T_{w_i}}^{T_{s_i}} K(T)\, dT = q_{s_i}\, x_{s_i} - \rho_{f_i}\, c_{p_f}\, \frac{x_{s_i}^2}{6}\left[\frac{\partial T_{w_i}}{\partial t} + 2\frac{\partial T_{s_i}}{\partial t}\right], \qquad (27)$$

An implicit numerical integration scheme was chosen to calculate $T_{s_i}$ for two reasons. The first is that $T_{s_i}$ is influenced much more by the changes in $\rho_{f_i}$ and $x_{s_i}$ than by changes in the internal enthalpy rate. Secondly, an order of magnitude analysis shows that at frost initiation time the first two terms in the above equation are much larger than the third term. This means an explicit numerical integration of the term $\frac{\partial T_{s_i}}{\partial t}$ is computationally inefficient because the roundoff errors will degrade the values of $\frac{\partial T_{s_i}}{\partial t}$ at the onset of frost formation.

Thus the term is approximated by:

$$\frac{\partial T_{s_i}}{\partial t} = (\ T_{s_i}^{\ t} - T_{s_i}^{\ t-\Delta t}\ )/\Delta t.$$  (28)

The parameters $\frac{dT_w}{dt}$ and $T_w$ are obtained from Equation (3) with the appropriate additional terms. Then using the same numerical techniques described by Dietenberger [5], the frost surface temperature is derived. Finally, the frost density and thickness are calculated using the same procedure as in Dietenberger [5].

The frost surface blackbody emissivity, $\varepsilon_{fr}$, needed as input to Equation (20), is related to the fraction of the frost surface in interaction with the radiation as given by:

$$\varepsilon_{fr} = (1 - B_i)\left[\varepsilon_{ice} + (\varepsilon_{Ale} - \varepsilon_{ice})e^{-10^5(x_{I_i} + x_{s_i})}\right].$$  (29)

This equation is similar to Equation (17) which takes into account the emissivity of the combined aluminum and frost/ice structure. Likewise, the solar absorptivity which replaces $\alpha_{fr}$ in Equation (20) is given by:

$$\alpha_{fr} = (1 - B_i)\left[\alpha_{ice_s} + (\alpha_{Al_s} - \alpha_{ice_s})e^{-10(x_{I_i} + x_{s_i})}\right].$$  (30)

Admittedly, the radiation model is idealized because radiation heat transfer actually occurs throughout the frost layer rather than just at the surface. If, however, we take typical nocturnal frost thicknesses of .1 to 10 mm, then according to Equation (29), the blackbody emissivity is mostly that of ice, and according to Equation (30), solar absorptivity is mostly that of the aluminum surface, which seems to agree with observations.

According to Dietenberger [5], if the frost surface temperature, $T_{s_i}$, rises to a critical temperature at which the water droplets forming on the frost surface do not have time to

freeze, but, instead, seep into the frost layer, then all the moisture arriving at the frost surface during a time increment will be assumed to totally result in the densification of the frost. Thus the densification rate above the critical temperature, but at or below the freezing temperature, is described as:

$$\frac{\partial \rho_{f_i}}{\partial t} = \frac{h_{M_i}}{x_{s_i}} ( \omega_a - \omega_{s_i} ),$$ (31)

while the frost thickness remains constant during the next time increment. Preliminary results of using Equation (27) for nocturnal frost formation indicates the temperature difference between the wall and the frost surface is typically a fraction of a degree. With this kind of small temperature difference, it appears the water seepage temperature will never be reached until the frost surface temperature is practically at the freezing temperature. Thus for nocturnal frost formation, the critical temperature or the water seepage temperature is set at the freezing temperature.

If the frost density finally reaches the ice density via the diffusion and the water seepage processes, and if the frost surface temperature as determined by Equation (27) remains below freezing, then the frost is allowed to continue to grow in frost thickness, but the frost density is held constant at the ice density. That is, we have, for the frost thickness as:

$$x_{s_i} = \int_0^t h_{M_i} ( \omega_a - \omega_{s_i} ) \, dt / \rho_I.$$ (32)

If by Equation (27) the frost surface temperature goes above the freezing temperature, and if the frost density is the same as the ice density, then the frost surface will begin melting and liquid water will run off. In this case, the frost surface temperature will remain at the freezing temperature, the frost density will remain a constant (that of ice), and the frost thickness will

decrease according to how much liquid water runs off. Thus the
decrease rate in the frost thickness is calculated by:

$$
\frac{-\partial x_{s_i}}{\partial t}\rho_{f_i} = \frac{1}{L_w}\{h_{H_i}(T_a - T_{s_i}) + h_{M_i} L_e(\omega_a - \omega_{s_i}) + \alpha_{fr} J_s
$$

$$
+ \sigma\varepsilon_{fr_e}\left[T_\infty^4(1 - F_e) + \left(\varepsilon_e T_e^4 + (1 - \varepsilon_e) T_\infty^4\right) F_e - T_{s_i}^4\right]
$$

$$
- \int_{T_{w_i}}^{T_{s_i}} K(T)\, dT/x_{s_i}\} \tag{33}
$$

where $T_{s_i}$ is set equal to 273.16.

## 2.3 MODELING NOCTURAL FROST FORMATION ON A FLAT PLATE

In validating the noctural frost formation model, an airfoil
geometry was inconvenient for various reasons. Since the testing
was to be done on a roof of a research building, the blackbody
radiation from the roof and the nearby shed would have been quite
difficult to evaluate at various view angles. Secondly, it was
beyond our existing measurement capabilities to measure local
wall temperature and local frost weight for different airfoil
panels. To simplify the problem of experimental validation, yet
provide useful results, a flat plate lying on a styrofoam box
inclined at an 15° angle was utilized. Thus the blackbody
radiation was coming from the sky and the earth, and the thermal-
couples could be attached underneath the plate. Only a single
mean frost weight measurement was needed. The flat plate design
then allowed a simplified analysis of the heat and mass transfer
coefficients and of the nocturnal frost formation modeling.
Although the flat plate has only a single blackbody view factor
and simplified flat plate equations, the main purpose here was to
verify the physical processes modeled within the frost layer from
which the frost weight and thickness were calculated.

When we are not dealing with a complicated geometry such as
the wing section, but, instead, with just a simple plate at a

uniform temperature, there is a very simple method of calculating the plate temperature. The heat balance of the plate itself is given by:

$$\rho_{Al}\, c_{P_{Al}}\, W\, \frac{dT_w}{dt} = q + \sigma \varepsilon_{plate} [T_\infty^4 (1 - F_e) + (\varepsilon_e\, T_e^4$$

$$+ (1 - \varepsilon_e)\, T_\infty^4)\, F_e - T_s^4] + \alpha_{plate}\, J_{sun} \qquad (34)$$

where:

$$\varepsilon_{plate} = B[\varepsilon_{ice} + (\varepsilon_{Al_e} - \varepsilon_{ice})\, e^{-10^5 x_I}] \text{ and}$$

$$\alpha_{plate} = B[\varepsilon_{ice_s} + (\varepsilon_{Al_s} - \varepsilon_{ice_s})\, e^{-10 x_I}].$$

Combining this equation with Equation (26) we obtain:

$$\frac{dT_w}{dt} = [q_s + \sigma \varepsilon_{plate} [T_\infty^4 (1 - F_e) + (\varepsilon_e\, T_e^4 + (1 - \varepsilon_e)\, T_\infty^4)\, F_e - T_s^4]$$

$$+ \alpha_{plate}\, J_{sun} - \rho_f\, c_{P_f}\, x_s\, \frac{\partial T_s}{\partial t}] / [\rho_{Al}\, c_{P_{Al}}\, W + \rho_f\, c_{P_f}\, x_s / 2] \qquad (35)$$

If Equation (35) is combined with Equation (20), then we obtain the same results as Equation (3) with the added terms but without thermal conduction terms. Thus an equally good alternative expression for $\frac{dT_w}{dt}$ to Equation (3) is given by Equation (35) for a single plate only. Substitution into Equation (27) from Equation (35) and Equation (28) provides complete information necessary to calculate the frost surface temperature, and, thus, also the frost thickness and density. A predictor-corrector scheme was used to integrate Equation (35) to obtain the plate temperature as a function of time. To validate the nocturnal frost formation model, comparisons were made with experiments on a slightly inclined plate exposed to nocturnal frost formation, as discussed further in a later section.

# SECTION 3

## MODELING OF THE HEAT AND MASS TRANSFER COEFFICIENTS

Given the complicated nature of calculating the nocturnal
frost formation, it was desired to use the simple yet suf-
ficiently accurate heat and mass transfer coefficients. The air
flow regimes over a wing section were examined to see if some
simple boundary layer technique could be utilized.

### 3.1 FORCED CONVECTION

For a wind flowing in the chordwise and the spanwise direc-
tion over a wing section, the criterias for boundary layer tran-
sition and for the boundary layer tripping can be evaluated.
Jacobs and Sherman [10] show some results for the characteristics
of an airfoil section as affected by variations in the Reynolds
number. The various airfoils examined generally retained a lami-
nar flow behavior up to a chord Reynolds number of about $5 \times 10^5$.
If the maximum wind speed for frost formation is taken to be
5 m/s and the average chord length of a general aviation wing is
taken as 1.5 m, then the chord Reynolds number is about $5 \times 10^5$.
This means the typical wind air flow over the smooth wing in the
chordwise direction is fully laminar. According to Biguria and
Wenzel [11], boundary layer tripping for turbulence induction.
occurs on a flat plate with a frost layer when the roughness
Reynold's number:

$$Re_{x_s} = \frac{U_\infty \, x_s}{\nu} \geqslant 1200. \tag{36}$$

Again, taking the maximum wind speed as 5 m/s, the frost
thickness would have to be greater than 3.6 mm for boundary layer
tripping to occur. A typical nocturnal frost thickness is less
than this, which means the boundary layer tripping is not
expected on the wing section covered with frost. Thus the

boundary layer in the chordwise direction will remain laminar for the nocturnal frost formation and a simple procedure for calculating the laminar heat tranfer coefficient obtained from Frick and McCullough [12] was used. Frick and McCullough validated their method on a NACA 65A015 airfoil which is fairly representative of many general aviation airfoils. The laminar forced convective heat transfer coefficient equation is:

$$h_x = 0.700 \ k_a / \delta_L \quad \text{and} \tag{37}$$

$$\delta_L = c \sqrt{\frac{5.3}{Re_c} \left(\frac{U_\infty}{U_e}\right)^{9.17} \int_0^{s/c} \left(\frac{U_e}{U_\infty}\right)^{8.17} d\left(\frac{s}{c}\right)} \tag{38}$$

The heat transfer coefficient at the stagnation point is based on that of a cylinder and is obtained from the <u>Handbook of Heat Transfer</u> [7] as:

$$h_x = \frac{0.57 \ c_p}{Pr^{0.6}} \left(\mu_e \ \rho_e \ \frac{dU_e}{ds}\right)^{1/2} \tag{39}$$

The potential flow code developed by Bristow [13] was used to calculate the potential flow velocities, $U_e$, around the airfoil. This potential flow code allows us to take into account the wind blowing from either the front or from the rear direction over the airfoil.

To consider the case of wind blowing from the side of the aircraft, or across the wing span, classical results of boundary layer analysis for a flat plate were used. The heat transfer coefficient is correlated in terms of the non-dimensional Nusselt number from the <u>Handbook of Heat Transfer</u> [7] as:

$$Nu_x = 0.332 \ Re_x^{1/2} \ Pr^{1/3} \quad \text{for Re} < 3.4 \times 10^5 \tag{40}$$

and:

$$Nu_x = St_x \ Re_x \ Pr \tag{41}$$

$$\frac{c_f/2}{St_x} = 0.9\left\{1 + 5\sqrt{\frac{c_f}{2}} \left\{0.0897467 + \left(\frac{Pr}{.9}-1\right) + \ln\left[1 + \frac{5}{6}\left(\frac{Pr}{.9} -1\right)\right]\right\}\right\} \tag{42}$$

$$c_f/2 = 0.185/(\log_{10} Re_x)^{2.584} \quad \text{for Re}_x > 3.4 \times 10^5. \tag{43}$$

The mass transfer coefficient in forced convection is obtained from the Chilton-Colburns analogy recommended by Dietenberger [5] for laminar and turbulent forced convection over a smooth and marginally rough frost surface. The analogy is:

$$Nu_x = Sh_x \, Le^{1/3} \qquad\qquad (44)$$

or: 
$$h_H/h_M = c_p \, Le^{-1/3} \qquad\qquad (45)$$

where Le is the Lewis number.

## 3.2 NATURAL CONVECTION

When the wind speed is low enough, natural convection will dominate the flow on the wing. That is, when the wing section surface is cooled below the ambient temperature by nocturnal radiation, the air adjoining the wing section is also cooled and will start flowing due to the heavier air mass of the cooled air. The Nusselt and the Sherwood numbers for a fairly horizontal plate (that is, the wing section angle of attack less than approximately 5 degrees) are given by:

$$Nu_c = 0.27 \, (Gr_c \, Pr)^{1/4} \qquad\qquad (46)$$

$$Sh_c = 0.10 \, (Gr_c \, Sc)^{1/4} \qquad\qquad (47)$$

where $Gr_c$ is the Grashof number based on chord length. The constant 0.27 was obtained from the Handbook of Heat Transfer [7] and the constant 0.10 is a fit to Tajama, et.al. [14] data for frost formation on a horizontal flat plate. The natural convection for an inclined plate (that is, the wing section angle of attack greater than approximately 5°) was analyzed by Dietenberger [5] and is reproduced in Appendix II for obtaining the Nusselt and the Sherwood numbers differently than Equations (46) and (47).

## 3.3 MIXED CONVECTION

When the heat and mass transfer coefficients from both the forced and natural convection equations are about equal, the air flow is in a mixed convection regime. Churchill [15] recommended for the cases of aiding flows where the forced air flow is in the same direction as the natural air flow, the mixed convection transfer coefficient, or equivalently, the Nusselt and Sherwood numbers, are well correlated by:

$$Nu_{mixed} = \left( (Nu_{forced})^3 + (Nu_{natural})^3 \right)^{1/3}, \tag{48}$$

with the similar equation for the Sherwood number. For the opposing flows, the mixed convection Nusselt number was correlated as:

$$Nu_{mixed} = \left| (Nu_{forced})^3 - (Nu_{natural})^3 \right|^{1/3}, \tag{49}$$

and in a likewise manner for the Sherwood number. When the forced convection flow is perpendicular to the natural convection flow, or when the plate is horizontal, the mixed convection Nusselt number is taken as the maximum of $Nu_{forced}$ or $Nu_{natural}$ and in a likewise manner for the Sherwood number.

For comparison of model results to the nocturnal frost experiments on a 15° inclined and 40 cm x 40 cm flat plate, the mean Nusselt and Sherwood numbers were derived from Equation (40), Appendix II, and Equation (48).

# SECTION 4

## COMPARISON OF THE NOCTURNAL FROST FORMATION PREDICTION
## TO EXPERIMENTS

To validate the nocturnal frost formation model, fourteen sets of experiments, seven of which formed nocturnal frost, were conducted by UDRI in the winter of 1981. The experimental apparatus consisted of two 40 cm x 40 cm square aluminum plates placed on two separate styrofoam boxes. The styrofoam boxes were designed to minimize any heat flux to the underneath side of the plate. Each plate sat at a 15° inclined angle from the horizontal. Fifteen degrees was chosen for the following reasons. According to the results by Sparrow, et.al., [16] for the forced convection regime, the average Nusselt number for a flat plate inclined at an angle of fifteen degrees should be equivalent to the average Nusselt number of the same plate in a horizontal position. Secondly, the experiments were performed on the roof of a building with an observation shed nearby. Thus, it was possible to orient the plate away from the building and minimize radiation heating from the building itself. No similar experiment on a wing section was conducted.

On one plate three very small thermocouples were attached underneath and were used to measure the plate temperature. Underneath the other plate was a weight measurement transducer. Periodically, the weight of the plate with frost was measured by temporarily placing a large styrofoam box over the plate to minimize the weight errors due to gusty winds. The frost thickness was measured on both plates with a penetrometer. The emissivity of the plate was found to be 0.2. This value was derived from a combination of infrared camera and thermocouple measurements on the plate. Along with the observations of plate temperatures, frost weight and thickness, the meteorological parameters were measured nearby. The wind speed was measured with a sensitive

hot-wire probe, the air temperature and relative humidity with a hygro-thermograph, and the pressure by a microbarograph. The degree of cloud cover and cloud types were estimated by visual observation. These meteorological observations are shown in Tables I to VII as a function of time. The blackbody sky radiation temperature given by Equation (6) is functionally related to the air temperature measured 1.5 meters from the ground rather than at the building height. Thus a correction was made to convert the observed air temperature at the top of the building to an equivalent 1.5 meter temperature. Only seven of the fourteen experimental data resulted in nocturnal frost formation. Results of these seven tests are presented in Tables I-VII and Figures 3-9.

The input data from Tables I-VII was used in the nocturnal frost formation model to generate a set of frost prediction curves as a function of time. These curves are compared to the actual frost measurements in Figures 3-9. The point symbols are the observed values. The open circles represent the measured plate temperature, and the solid lines correspond to model predictions of plate temperatures. The open triangles correspond to the frost weight measurements, and the dashed curves correspond to model prediction of the frost weight. Lastly, the open squares correspond to the frost thickness measurements, and the dot-dashed curves correspond to the model predictions of the frost thickness. Frost thickness measurements were not made on the first data set.

Although the thermocouple measurements are accurate within a few-tenths, of a degree Celsius, the variability in the wind speeds has caused temperature measurement oscillations as high as 2.6°C and about 1°C on the average. When Figures 3 to 9 are examined, the predicted plate temperatures prior to frost initiation show agreement with the data within a random error of 1 to 2°C.

TABLE I

Meteorology Data Collected During Frost Formation Experiment #4
and Converted to Metric Units.

| HOURS | TIME (SEC) | AIR TEMPERATURE (DEG K) | RELATIVE HUMIDITY | AIR SPEED (M/SEC) | PRESSURE (J/M**3) | FRACTION OF CLOUD COVER (CLEAR) |
|---|---|---|---|---|---|---|
| 10:30 P.M. | 0 | 272.60 | 0.75 | 1.03 | 99110 | 0.0 |
| 11:30 P.M. | 3600 | 273.16 | 0.78 | 1.03 | 99110 | 0.0 |
| 12:30 A.M. | 7200 | 273.16 | 0.88 | 1.54 | 99110 | 0.0 |
| 1:30 A.M. | 10800 | 274.27 | 0.90 | 1.03 | 99110 | 0.0 |
| 2:30 A.M. | 14400 | 273.16 | 0.88 | 1.03 | 99110 | 0.0 |
| 4:00 A.M. | 19800 | 272.60 | 0.89 | 2.06 | 99110 | 0.0 |
| 5:00 A.M. | 23400 | 273.16 | 0.88 | 2.57 | 99110 | 0.0 |

TABLE II

Meteorology Data Collected During Frost Formation Experiment #6
and Converted to Metric Units.

| HOURS | | TIME (SEC) | AIR TEMPERATURE (DEG K) | RELATIVE HUMIDITY | AIR SPEED (M/SEC) | PRESSURE (J/M**3) | FRACTION OF CLOUD COVER (CLEAR) |
|---|---|---|---|---|---|---|---|
| 11:00 | P.M. | 0 | 277.60 | 0.64 | 1.54 | 99750 | 0.0 |
| 2:00 | A.M. | 10800 | 275.38 | 0.70 | 0.69 | 99750 | 0.0 |
| 3:00 | A.M. | 14400 | 275.38 | 0.70 | 0.56 | 99750 | 0.0 |
| 4:30 | A.M. | 19800 | 274.27 | 0.72 | 0.77 | 99750 | 0.0 |
| 5:30 | A.M. | 23400 | 273.16 | 0.80 | 0.41 | 99750 | 0.0 |

**TABLE III**

Meteorology Data Collected During Frost Formation Experiment #7
and Converted to Metric Units.

| HOURS | | TIME (SEC) | AIR TEMPERATURE (DEG K) | RELATIVE HUMIDITY | AIR SPEED (M/SEC) | PRESSURE (J/M**3) | FRACTION OF CLOUD COVER (CIRROSTRATUS) |
|---|---|---|---|---|---|---|---|
| 9:40 | P.M. | 0 | 274.27 | 0.570 | 1.02 | 100400 | 0.6 |
| 10:30 | P.M. | 3000 | 274.27 | 0.570 | 2.54 | 100370 | 0.6 |
| 12:45 | A.M. | 11100 | 273.16 | 0.680 | 1.27 | 100270 | 0.0 |
| 2:10 | A.M. | 16200 | 273.16 | 0.670 | 2.54 | 100240 | 0.0 |
| 3:00 | A.M. | 19200 | 273.16 | 0.660 | 2.29 | 100240 | 0.0 |
| 4:00 | A.M. | 22800 | 272.60 | 0.660 | 2.00 | 100240 | 0.0 |
| 5:00 | A.M. | 26400 | 272.60 | 0.690 | 1.70 | 100200 | 0.0 |
| 6:00 | A.M. | 30000 | 272.05 | 0.810 | 1.41 | 100200 | 0.0 |
| 7:20 | | 34800 | 269.83 | 0.810 | 1.20 | 100170 | 0.0 |
| 7:40 | | 36000 | 269.83 | 0.810 | 1.20 | 100140 | 0.0 |

## TABLE IV

Meteorology Data Collected During Frost Formation Experiment #8
and Converted to Metric Units.

| HOURS | TIME (SEC) | AIR TEMPERATURE (DEG K) | RELATIVE HUMIDITY | AIR SPEED (M/SEC) | PRESSURE (J/M**3) | FRACTION OF CLOUD COVER (STRATUS) |
|---|---|---|---|---|---|---|
| 9:25 P.M. | 0 | 277.05 | 0.73 | 2.21 | 98200 | 0.1 |
| 10:55 P.M. | 4200 | 276.49 | 0.80 | 2.21 | 98200 | 0.5 |
| 11:45 P.M. | 8400 | 276.22 | 0.80 | 2.21 | 98270 | 0.0 |
| 12:45 A.M. | 12000 | 275.94 | 0.81 | 2.01 | 98270 | 0.0 |
| 1:45 A.M. | 15600 | 275.94 | 0.82 | 2.21 | 98270 | 0.4 |
| 2:45 A.M. | 19200 | 275.66 | 0.82 | 2.00 | 98270 | 0.7 |
| 3:45 A.M. | 22800 | 275.38 | 0.82 | 1.75 | 98330 | 0.0 |
| 4:45 A.M. | 26400 | 275.38 | 0.83 | 1.75 | 98400 | 0.0 |
| 5:30 A.M. | 29100 | 275.38 | 0.83 | 1.34 | 98400 | 0.0 |
| 6:10 A.M. | 31500 | 274.27 | 0.84 | 0.87 | 98470 | 0.0 |
| 6:40 A.M. | 33300 | 274.27 | 0.93 | 0.87 | 98500 | 0.0 |
| 7:15 A.M. | 35400 | 273.99 | 0.93 | 0.41 | 98530 | 0.0 |
| 7:40 A.M. | 36900 | 274.27 | 0.90 | 0.41 | 98530 | 0.0 |

TABLE V

Meteorology Data Collected During Frost Formation Experiment #9
and Converted to Metric Units.

| HOURS | TIME (SEC) | AIR TEMPERATURE (DEG K) | RELATIVE HUMIDITY | AIR SPEED (M/SEC) | PRESSURE (J/M**3) | FRACTION OF CLOUD COVER (CLEAR) |
|---|---|---|---|---|---|---|
| 12:15 A.M. | 0 | 274.55 | 0.84 | 3.00 | 98930 | 0.0 |
| 1:15 A.M. | 3600 | 274.27 | 0.86 | 3.09 | 98930 | 0.0 |
| 2:15 A.M. | 7200 | 273.16 | 0.88 | 2.50 | 99000 | 0.0 |
| 2:45 A.M. | 9000 | 273.16 | 0.88 | 2.01 | 99000 | 0.0 |
| 3:20 A.M. | 11100 | 273.16 | 0.88 | 2.00 | 99000 | 0.0 |
| 3:50 A.M. | 12900 | 272.88 | 0.88 | 3.19 | 99000 | 0.0 |
| 4:30 A.M. | 15300 | 272.33 | 0.88 | 2.88 | 99070 | 0.0 |
| 5:15 A.M. | 18000 | 272.05 | 0.89 | 2.88 | 99100 | 0.0 |
| 6:00 A.M. | 20700 | 271.49 | 0.92 | 3.09 | 99170 | 0.0 |
| 6:45 A.M. | 23400 | 271.49 | 0.92 | 2.01 | 99200 | 0.0 |
| 7:15 A.M. | 25200 | 271.49 | 0.94 | 2.21 | 99230 | 0.0 |
| 7:30 A.M. | 26100 | 271.49 | 0.92 | 1.75 | 99230 | 0.0 |

## TABLE VI

Meteorology Data Collected During Frost Formation Experiment #11
and Converted to Metric Units.

| HOURS | | TIME (SEC) | AIR TEMPERATURE (DEG K) | RELATIVE HUMIDITY | AIR SPEED (M/SEC) | PRESSURE (J/M**3) | FRACTION OF CLOUD COVER (STRATUS) |
|---|---|---|---|---|---|---|---|
| 10:00 | P.M. | 0 | 273.16 | 0.88 | 1.00 | 99560 | 0.0 |
| 11:00 | P.M. | 3600 | 270.38 | 0.89 | 1.52 | 99560 | 0.0 |
| 12:00 | A.M. | 7200 | 271.22 | 0.89 | 1.52 | 99560 | 1.0 |
| 12:35 | A.M. | 9300 | 271.22 | 0.92 | 1.00 | 99594 | 0.0 |
| 1:05 | A.M. | 11100 | 270.94 | 0.93 | 0.81 | 99560 | 0.0 |
| 1:35 | A.M. | 12900 | 270.10 | 0.93 | 1.00 | 99560 | 0.4 |
| 2:05 | A.M. | 14700 | 269.83 | 0.95 | 1.50 | 99560 | 0.0 |
| 2:35 | A.M. | 16500 | 269.55 | 0.93 | 1.52 | 99560 | 0.0 |
| 3:10 | A.M. | 18600 | 269.83 | 0.91 | 0.76 | 99560 | 0.0 |
| 4:10 | A.M. | 22200 | 269.27 | 0.89 | 0.51 | 99526 | 0.0 |
| 5:10 | A.M. | 25800 | 268.72 | 0.88 | 1.00 | 99526 | 0.0 |
| 6:10 | A.M. | 29400 | 268.72 | 0.88 | 1.00 | 99560 | 0.0 |
| 6:15 | A.M. | 29700 | 268.72 | 0.88 | 1.00 | 99560 | 0.0 |

## TABLE VII

Meteorology Data Collected During Frost Formation Experiment #13
and Converted to Metric Units.

| HOURS | TIME (SEC) | AIR TEMPERATURE (DEG K) | RELATIVE HUMIDITY | AIR SPEED (M/SEC) | PRESSURE (J/M**3) | FRACTION OF CLOUD COVER (CIRROSTRATUS) |
|---|---|---|---|---|---|---|
| 12:20 A.M. | 0 | 273.16 | 0.75 | 1.52 | 98781 | 0.0 |
| 1:15 A.M. | 3300 | 272.05 | 0.75 | 1.52 | 98747 | 0.0 |
| 2:00 A.M. | 6000 | 272.05 | 0.75 | 1.52 | 98747 | 0.0 |
| 3:00 A.M. | 9600 | 271.77 | 0.78 | 0.76 | 98713 | 0.0 |
| 3:45 A.M. | 12300 | 272.33 | 0.77 | 0.76 | 98713 | 0.0 |
| 4:15 A.M. | 14100 | 272.60 | 0.78 | 0.71 | 98713 | 0.1 |
| 4:50 A.M. | 16200 | 270.94 | 0.80 | 0.51 | 98747 | 0.1 |
| 5:20 A.M. | 18000 | 270.38 | 0.83 | 0.66 | 98747 | 0.1 |
| 6:00 A.M. | 20400 | 270.66 | 0.82 | 0.46 | 98747 | 0.1 |
| 6:30 A.M. | 22200 | 270.38 | 0.82 | 0.51 | 98781 | 0.0 |

Figure 3.  Model Predictions and Data Measurements of Plate Temperature
and Frost Weight and Thickness as a Function of Time for
Frost Formation, Experiment #4.

Figure 4. Model Predictions and Data Measurements of Plate Temperature and Frost Weight and Thickness as a Function of Time for Frost Formation, Experiment #6.

Figure 5. Model Predictions and Data Measurements of Plate Temperature and Frost Weight and Thickness as a Function of Time for Frost Formation, Experiment #7.

Figure 6.   Model Predictions and Data Measurements of Plate Temperature
and Frost Weight and Thickness as a Function of Time for
Frost Formation, Experiment #8.

Figure 7. Model Predictions and Data Measurements of Plate Temperature and Frost Weight and Thickness as a Function of Time for Frost Formation, Experiment #9.
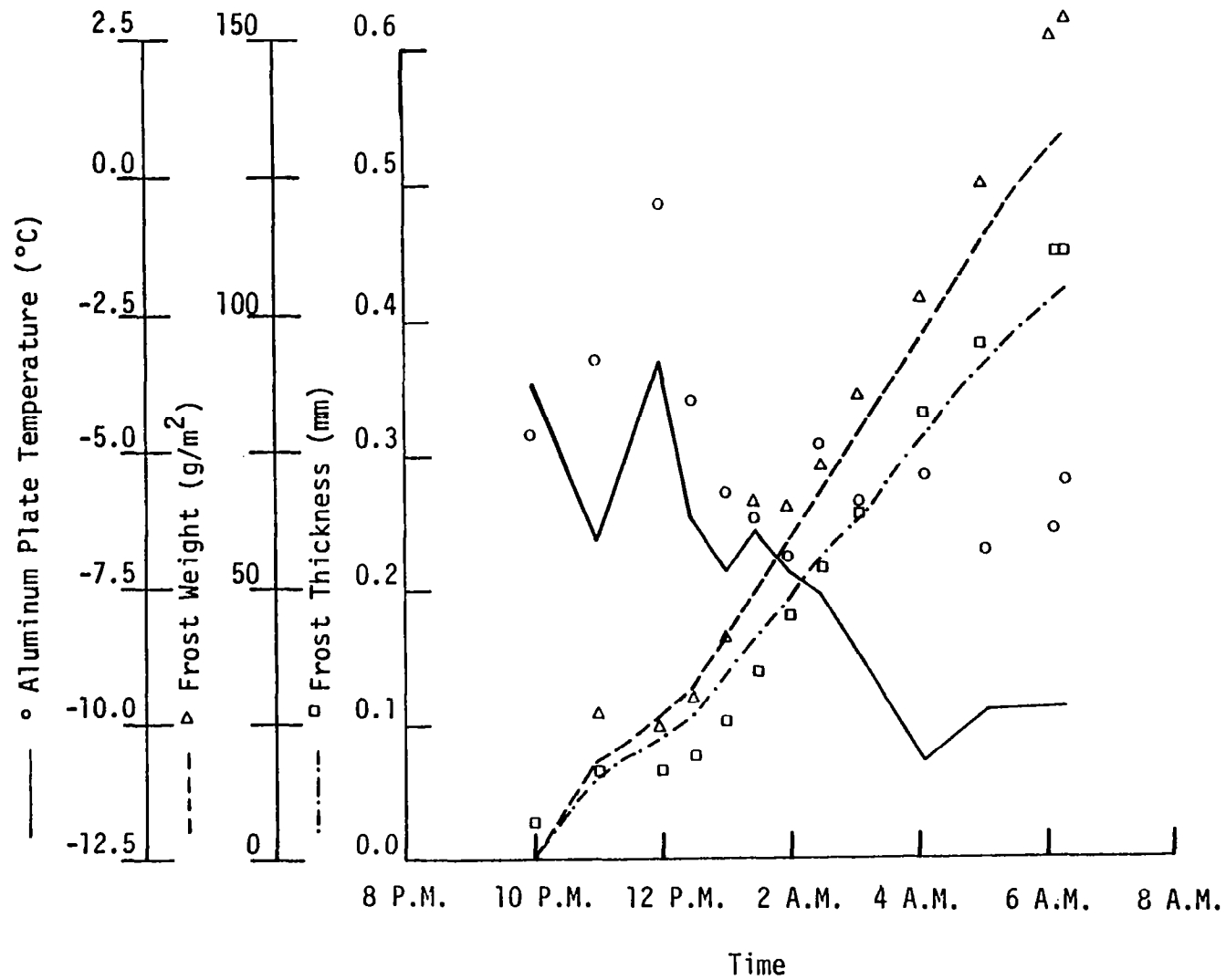
Figure 8. Model Predictions and Data Measurements of Plate Temperature
and Frost Weight and Thickness as a Function of Time
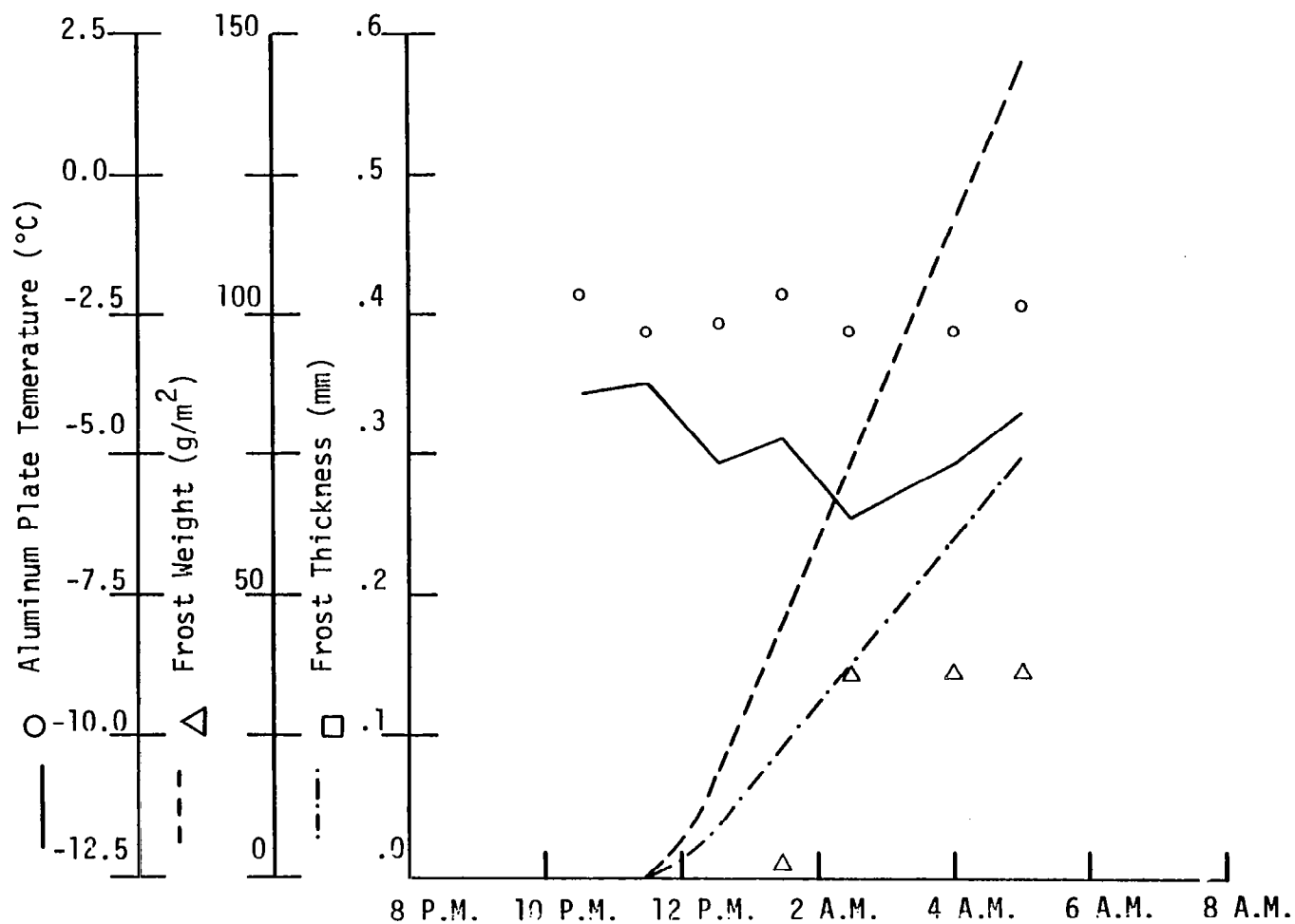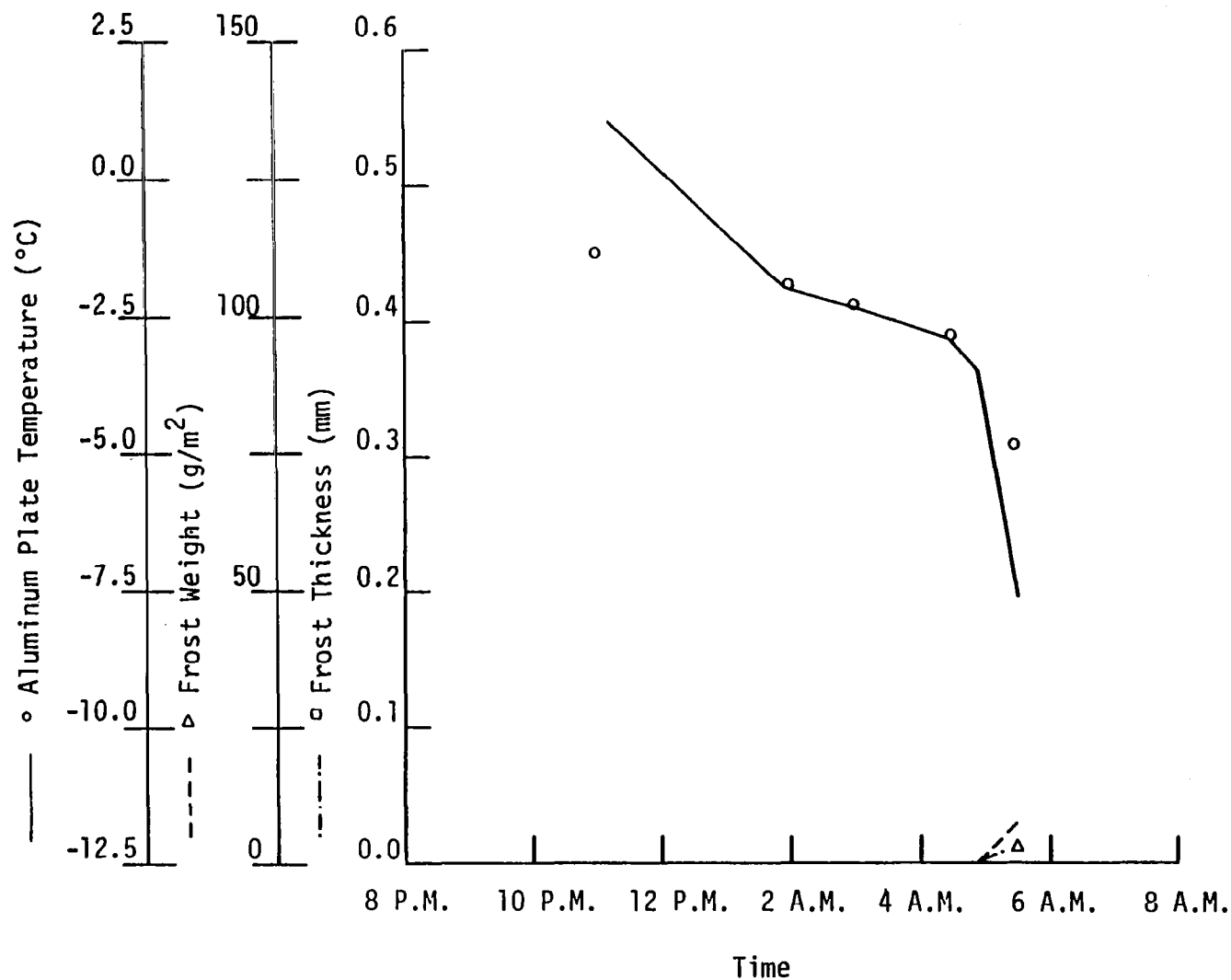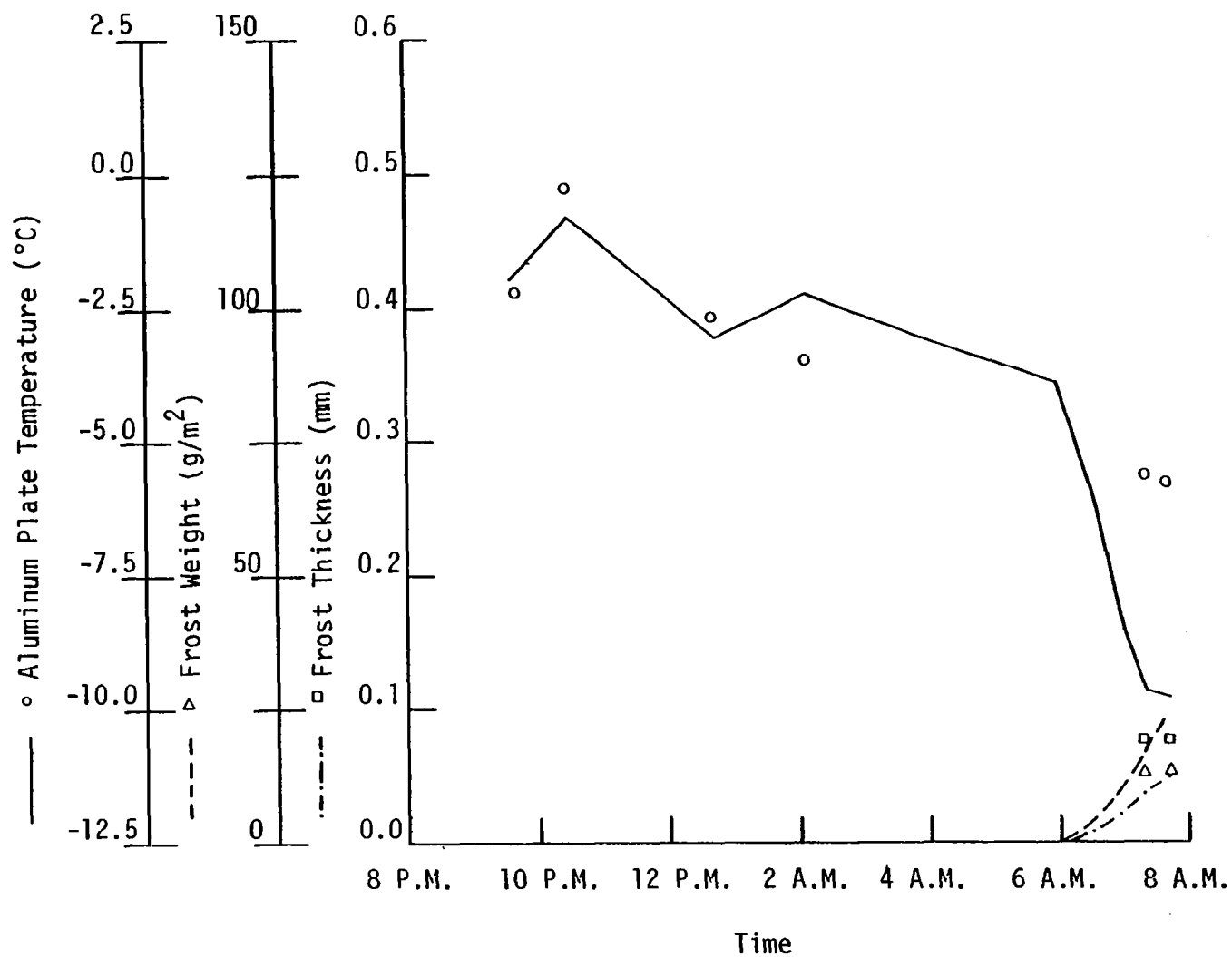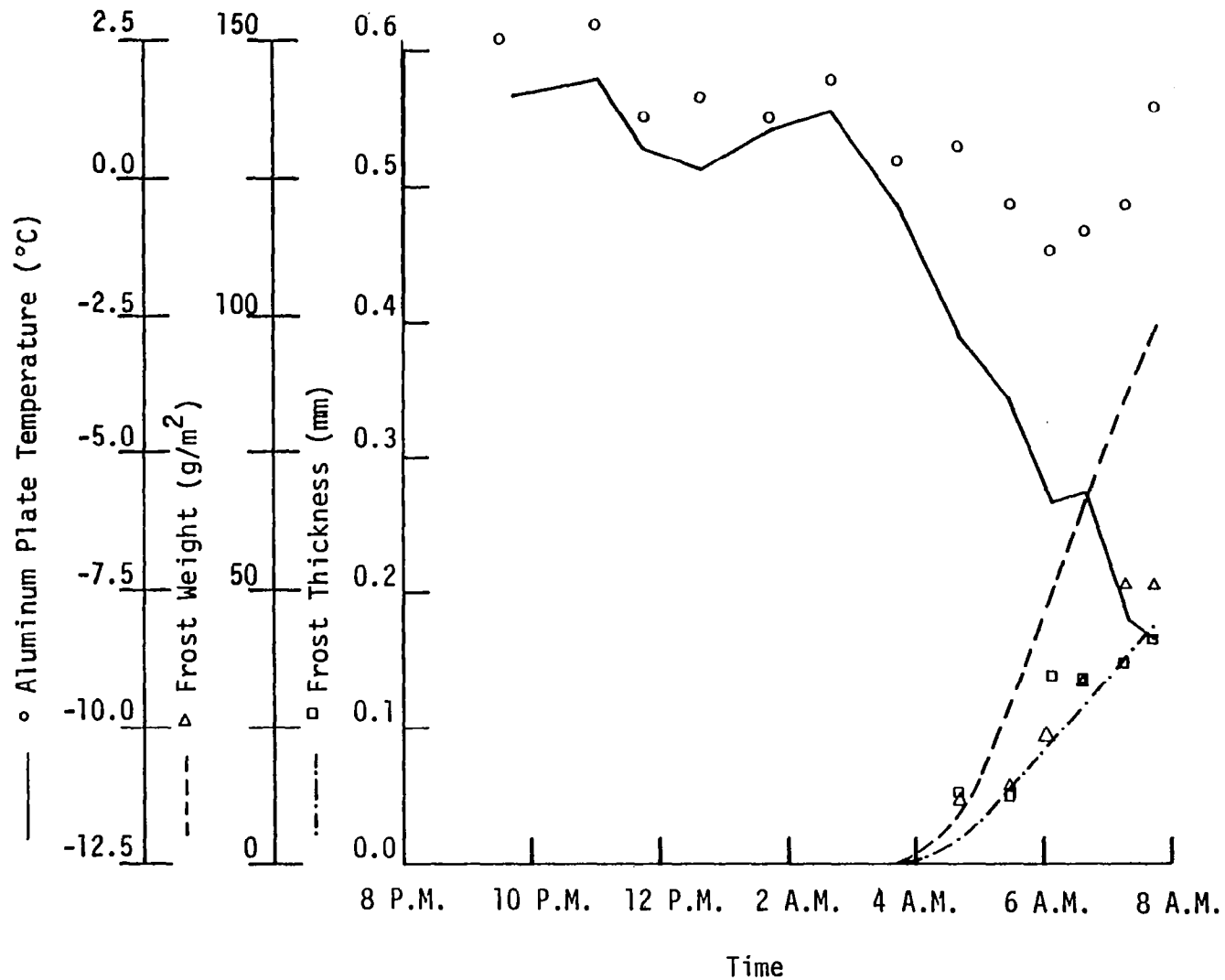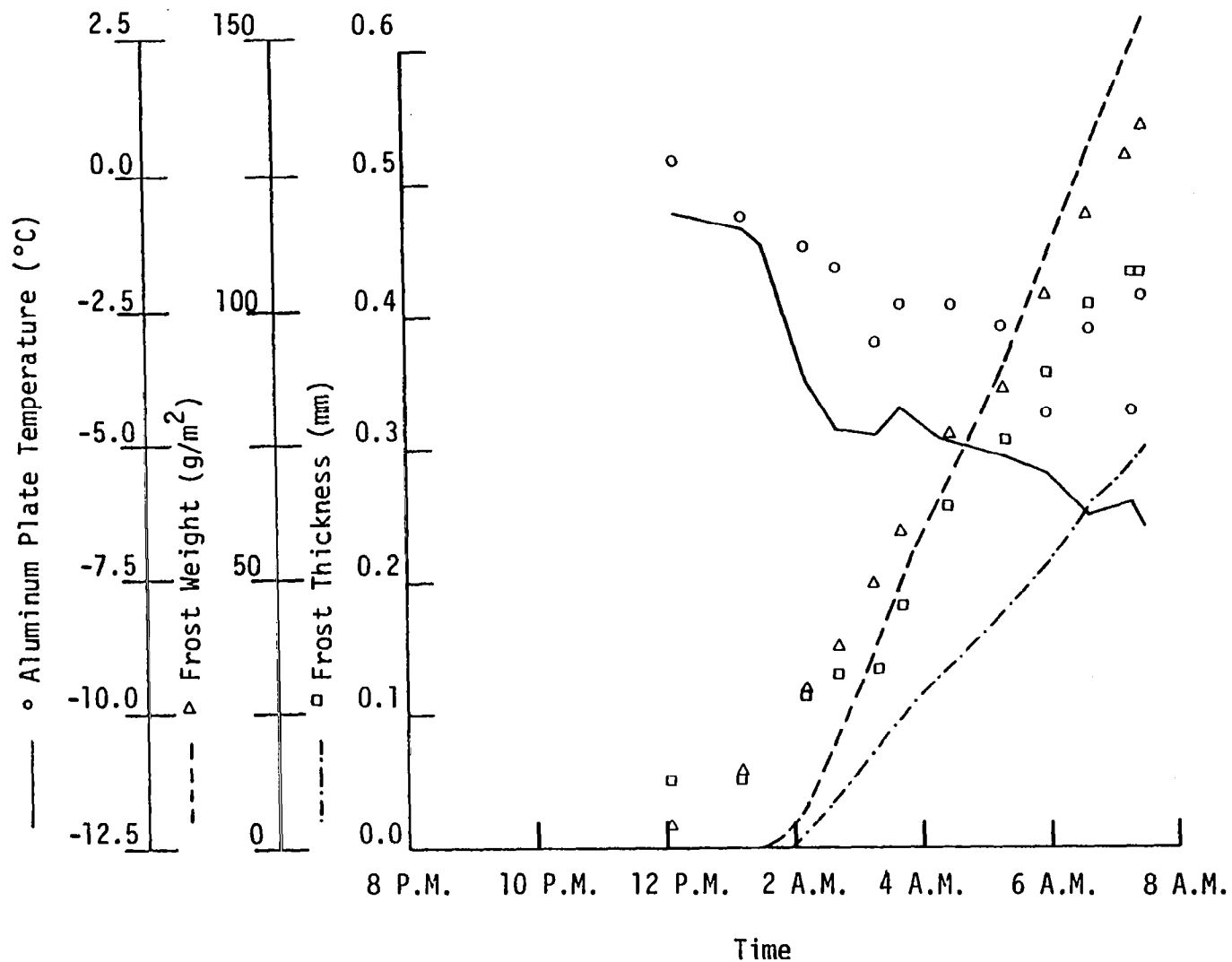for Frost Formation, Experiment #11.
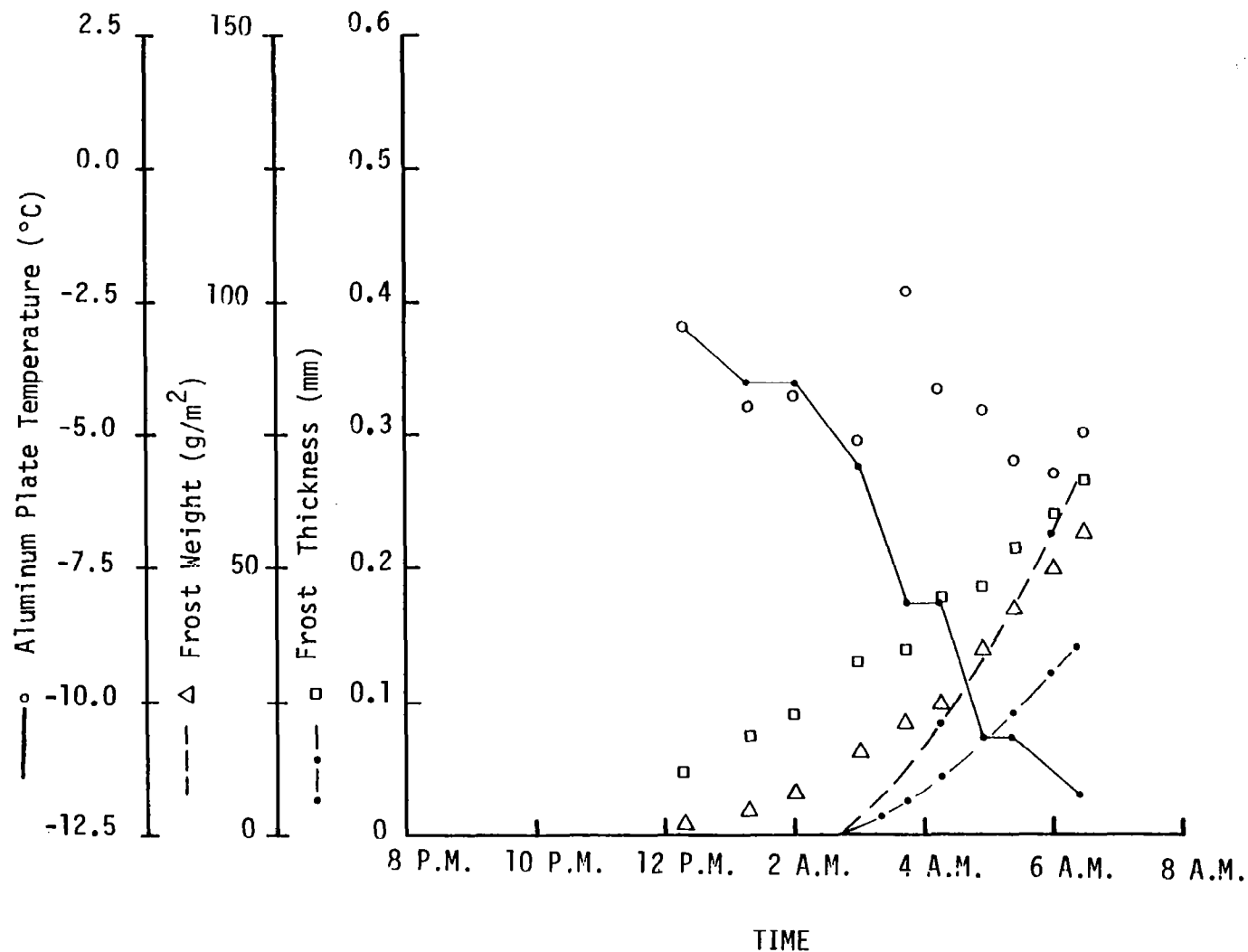
Figure 9.  Model Predictions and Data Measurements of Plate Temperature and Frost Weight and Thickness as a Function of Time for Frost Formation, Experiment #13.

On seven other data sets, not shown, where no frost formed at all, similar agreement was found. Once frost starts to form, the predicted plate temperatures tend to fall 2.5 to 5.0 degrees below the measured values. The more severe cases, (that is, the 5.0 degrees deviation) generally occurred near sunrise and can possibly be associated with solar radiation, which was not modeled for these data sets. Nevertheless, even before the onset of sunrise, there often exists a 2.5 degrees bias that needs explanation.

On the seven data sets where no frost formed at all, the model did not predict any frost formation. In Figures 4, 5, 6, and 8, the frost initiation occurred at the correct times as compared to the data, while in Figures 3, 7, and 9, the frost initiation was in error by less than two hours. Thus the frost initiation timing is good considering the oscillations in the plate temperature caused by the wind speed variability.

As can be seen from Figures 6 to 9, the accuracy of the frost weight and thickness measurements is so good that one can identify the shape of the frost weight and thickness curves versus time. In all Figures 3-9, except for Figure 8, the predicted frost weight tends to increase somewhat too rapidly and the predicted frost thickness is somewhat too low. This could be due to the predicted plate temperature being too cold since the vapor mass flux is in an inverse relationship to the plate temperature. The vapor mass flux is also proportional to the heat transfer coefficient, but decreasing the heat transfer coefficient would produce an even colder predicted wall temperature. If the heat transfer coefficient is increased instead so as to increase the predicted wall temperature, it may or may not reduce the vapor mass flux. There is, however, no other rationale to calculate the heat transfer coefficient different than a laminar plate air flow assumption. As was demonstrated in an earlier analysis, the

boundary layer transition or tripping is unlikely to occur over the frost layer to produce a turbulent flow on the plate that would give a higher heat transfer coefficient. The possibility of laminar boundary layer separation on the blunt styrofoam boxes is not feasible because the same wall temperature bias would have occurred in the non-frosted case. Thus the presence of frost is unlikely to affect the boundary layer over the test plates.

Allowing the plate wall to see more of the blackbody radiation and the frost surface to see less of the radiation in the modeling of the surface emissivity will increase the predicted wall temperature and decrease the predicted frost weight. However, the predicted frost thickness, already too low, would get even lower. A higher predicted sky temperature, perhaps due to a fog layer, would increase the predicted wall temperature, decrease the predicted frost weight, and perhaps increase the predicted frost thickness. Indeed, Figure 8 is an exception to the rule in providing good predictions of the frost weight and thickness which seems to indicate the wall temperature is predicted correctly and the surface emissivity model is sound. A further point can be made, that if there were systematic errors in the heat transfer coefficients or the emissivity model, then the same effect on the predicted wall temperature, frost weight and thickness as compared to the data should have appeared in all nocturnal frost formation experiments. However, the good results shown in Figure 8 have provided the exception among the experiments. An error in the sky temperature allows for exceptions, because the earth environment at 1.5 meters height may not correlate well with the temperatures and relative humidity measurements at building heights in some cases. Somewhat better agreement with the data may be obtained if the sky temperature is based directly on measurements of air temperature and relative humidity at 1.5 m height and the solar radiation taken into account. The code for the nocturnal frost formation on the

airplane wing as versus that on the plate has incorporated these improvements [17]. However, new experiments are needed to verify these improvements in the radiation flux to the surface, and to uncover any more systematic errors.

In summary, when the frost weight and thickness prediction versus the data are taken together from Figures 6 to 9, we find the predictions show the correct qualitative behavior and the values of the correct magnitudes. In one instance, in Figure 8, the agreement with the measured frost weight and thickness was very good. This indicates the blackbody radiation and the heat capacitance modeling of the nocturnal frost layer is a good approximation to the heat processes involved. As a first known model of its kind, the nocturnal frost formation model does quite well in spite of the approximations that were made to represent the flat plate experiments.

# SECTION 5

## AIRCRAFT TAKEOFF PERFORMANCE ANALYSIS

This section will evaluate the aerodynamic penalties associated with surface roughness on the aircraft, especially if the roughness is caused by nocturnal frost. The aircraft equations of motion for a steady climbing flight are then used to analyze modified takeoff procedures. Also, an analysis of how a pilot not aware of the dangers of frost can or cannot takeoff successfully is discussed in this section.

Ideally, a potential flow code interacting with a boundary layer code that adequately takes into account the presence of frost on a multi-element airfoil could be used to evaluate the lift and drag coefficients of an aircraft at takeoff speeds. Such a program does not presently exist. Thus wind tunnel data on the lift and drag penalties due to the upper wing surface roughness were examined. Brumby [3] developed some correlations for the relative loss in the maximum lift coefficient as a function of the average roughness height to chord ratio. Ljungstroem [2] measured lift and drag penalties for three configurations of the NACA 652A215 wing section as a function of angle of attack, simulated frost roughness height, Reynold's number, and the roughness chordwise distribution. The three configurations consisted of the basic wing shape, the wing section with 20° trailing edge flaps, and a wing with a high-lift leading edge device. The wing with the 20° trailing edge flaps is most representative of a general aviation aircraft at takeoff. As far as the actual frost roughness height is concerned, Dietenberger [5] has described the sand-grain roughness height as equivalent to or up to 66 percent greater than the frost thickness. The equivalent sand grain roughness generally does not depend on the frost density for a typical nocturnal frost layer.

The qualitative structure of frost roughness was simulated by Ljungstroem using standard aluminum oxide grinding paper. Three grades of roughness were used corresponding to roughness heights of 0.5, 0.1 and .05 mm. As will be shown in a later section, the nocturnal frost formation model predicts a frost thickness that tends to be uniform, but covers at times only a portion of the wing section. Thus using primarily Ljungstroem data, an empirical relationship was established for the drag and lift penalties due to the nocturnal frost formation on the wing at takeoff speeds. In Appendix III the empirical relationships of drag and lift penalties were developed for the NACA 652A215 wing section with the 20° flaps and a fuselage covered with simulated frost. For the same wing section, Figure 10 shows the resulting empirical relationship of lift coefficients versus angle of attack due to upper surface roughness in comparison to Ljungstroem's wind tunnel data. Figure 11, likewise, shows the empirical curves for the drag coefficient versus angle of attack due to upper surface roughness in comparison to Ljungstroem wind tunnel data. These figures are discussed further in Appendix III.

## 5.1 TAKEOFF TECHNIQUES WITH ROUGHENED AIRFOIL

Some researchers, knowing of the consequential takeoff performance degradation due to the aerodynamic penalties of a roughened airfoil, have suggested takeoff modification procedures to insure takeoff safety. According to Ljungstroem, "It would mean a substantial saving to the airlines if it was sufficient to clean only a small part of the wing and control surfaces (that is, from the leading edge and 10-20% backwards)." Weeks [4] had a significantly different approach:

> "While our knowledge of the detailed flow phenomena which are involved is still far from adequate, so that estimates such as these can only be tentative ones, it is concluded that some combination of take-off weight reduction and increase in take-off speed will be necessary in order to maintain the normal safety margins in the presence of hoar frost deposits."
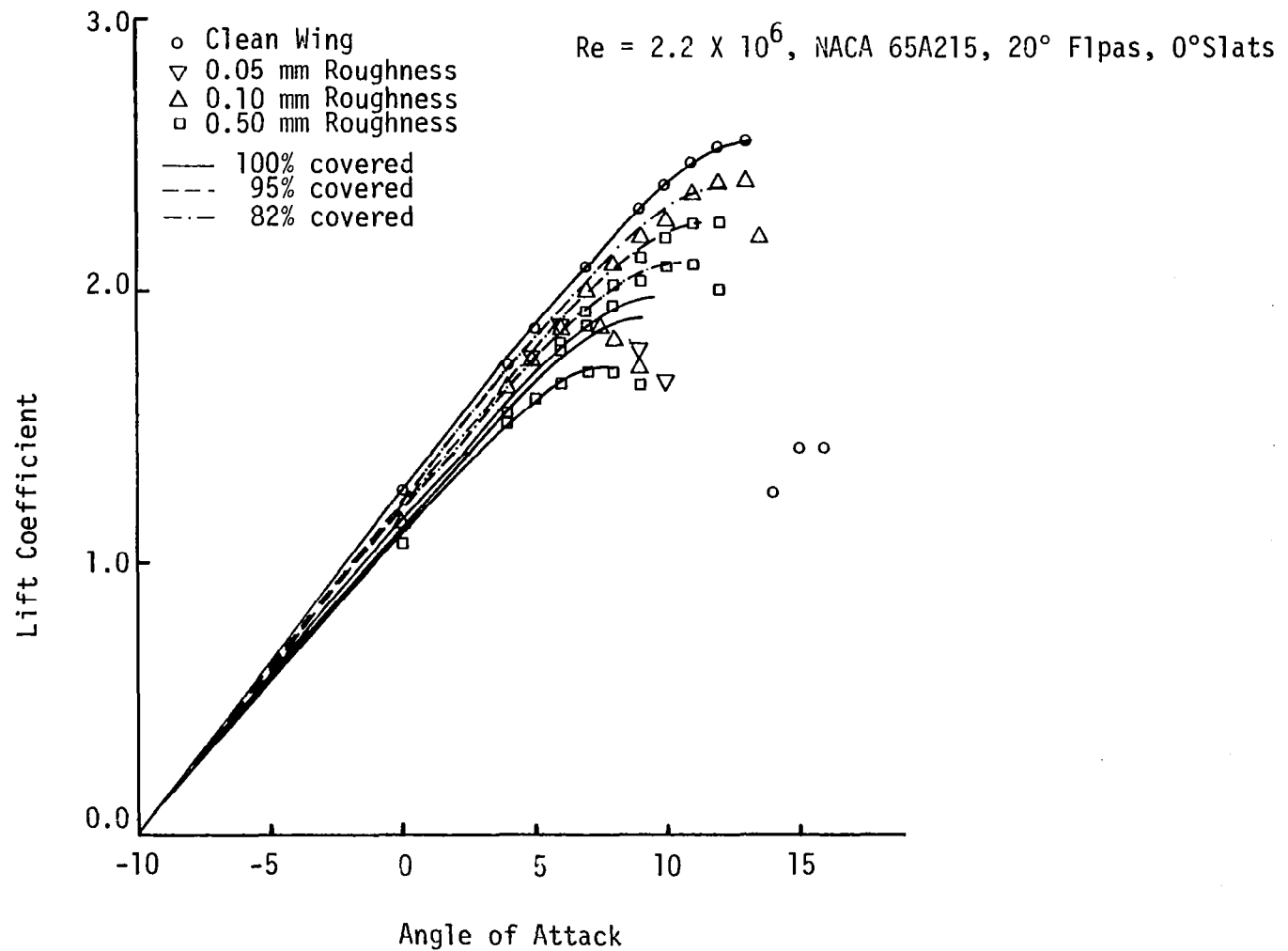
Figure 10. Empirical Curve of Lift Coefficients versus Angle of Attack due to Upper Surface Roughness in Comparison to Ljunstroem's Wind Tunnel Data.
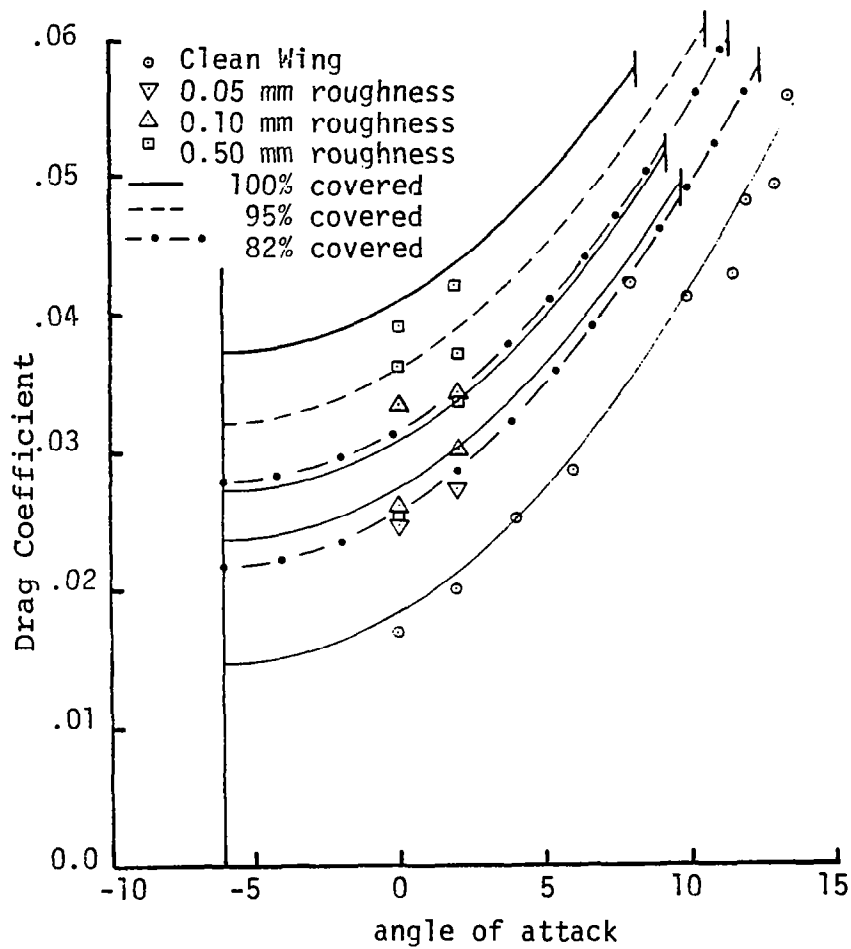
Figure 11. Empirical Curves for Drag Coefficients Versus Angle of Attack due to Upper Surface Roughness in Comparison to Ljungstrem's Wind Tunnel Data.

Finally, Galins and Shirkey's [18] specific recommendation for the Boeing 737 aircraft is:

"When takeoffs are executed during suspected icing conditions or adverse weather conditions, sound operational techniques must be exercised. Wings should be kept clear of ice and other forms of contamination and rotation rates should not exceed three degrees/second. If deemed necessary, improved climb performance (that is, 6% takeoff overspeed) may be used for added takeoff speed margins at any flap setting."

The following analysis evaluates each of the suggested modified takeoff procedures and, as a result, a new effective takeoff procedure is recommended.

To help evaluate the performance penalties at takeoff, it will be assumed the aircraft flies in a steady, linear, climbing trajectory after takeoff. It is also assumed that during the ground takeoff run, the thrust is much larger than the increased drag force due to roughness so that the extra runway length covered before takeoff is negligible. An approximated set of steady climbing flight equations are:

$$W\cos\gamma = C_L \left(\frac{\rho_a}{2}\right)Sv^2 \tag{50}$$

$$T - W\sin\gamma = C_D \left(\frac{\rho_a}{2}\right)Sv^2 \tag{51}$$

Assume that for any flight at takeoff, the thrust, the air density, and the wing area are constants. The lift and drag coefficients will vary according to the existence of frost on the wings and fuselage. The gross weights, the takeoff speed, and the trajectory angle are adjustable parameters. Let the subscript R stand for rough aircraft surface and the subscript c stand for clean aircraft surface. With this situation, Equations (50) and (51) are rewritten removing the thrust, density and wing area parameters as:

$$\frac{W_R \cos \gamma_R}{W_c \cos \gamma_c} = \frac{C_{L_R} V_R^2}{C_{L_c} V_c^2} = \left(1 - \frac{\Delta C_{L_c}}{C_{L_c}}\right)\frac{V_R^2}{V_c^2} \quad \text{and:} \qquad (52)$$

$$T = W_R \sin \gamma_R + C_{D_R}\left(\frac{\rho_a S}{2}\right)V_R^2 = W_c \sin \gamma_c + C_{D_c}\left(\frac{\rho_a S}{2}\right)V_c^2. \qquad (53)$$

Equations (52) and (53) relate parameters for steady state climbing with a roughened aircraft to those for a steady state climb with a clean aircraft. Equation (52), for example, implies that if a clean aircraft with weight $W_c$ is climbing at a climb angle $\gamma_c$, then for a roughened aircraft to have a constant climb angle of $\gamma_R$, the Equation (52) relationship must hold. In a similar fashion, for an aircraft with a given fixed amount of thrust in a steady state climbing conditions, the drag plus weight component in the direction opposite to the thrust must equal the thrust, for both clean aircraft and roughened aircraft configurations.

Considering the clean aircraft takeoff parameters, $W_c$, $\gamma_c$, $C_{L_c}$, $C_{D_c}$, $V_c$ are known and the roughened aircraft lift and drag curves ($C_{L_R}$, $C_{D_R}$) are available by modifying the clean aircraft curves. There remain three unknowns $W_R$, $V_R$, $\gamma_R$ and two equations. This allows us to assign a value to one of the variables and solve for the other two that result in a steady climbing flight.

The analysis was performed on a single engine, general aviation type aircraft described by Fink, et al. [19]. The typical aircraft parameter values for takeoff are given in Table VIII. For a $\gamma_c = 3.5°$ steady state climb angle, the necessary angle of attack and thrust are derived by solving Equations (50) and (51) using the lift and drag coeffcients curves versus angle of attack

TABLE VIII

Results of Takeoff Analysis for a Single Engine,
General Aviation Aircraft

$(\gamma_C=3.5, \ W_C=3100 \ lb, \ (\rho_a S/2)V_C^2 =2608.2, \ C=4.91 \ ft, \ l=25.28 \ ft)$

| k (mm) | P | $\Delta C_L/C_L$ | $\Delta\alpha/\alpha$ | $\Delta C_D$ | $\alpha_{takeoff}$ (degrees) | Galins & Shirley's $(W_R=W_C)$ | | Weeks' $(\gamma_R=\gamma_C)$ | | Author's $(V_R=V_C)$ | |
|---|---|---|---|---|---|---|---|---|---|---|---|
| | | | | | | $\gamma_R$ (degrees) | $V_R$ (ft/s) | $V_R$ (ft/s) | $(W_C-W_R)/W_C$ | $\gamma_R$ (degrees) | $(W_C-W_R)/W_C$ |
| 1.0 | 1.0 | 0.333 | 0.241 | 0.0274 | 4.69 | -0.66 | 132.6 | 107.2 | 0.346 | 3.26 | 0.333 |
| 0.5 | 1.0 | 0.304 | 0.220 | 0.0214 | 4.93 | -0.00 | 129.9 | 108.4 | 0.301 | 3.54 | 0.304 |
| 0.1 | 1.0 | 0.237 | 0.172 | 0.0096 | 5.49 | 1.37 | 124.1 | 110.7 | 0.202 | 3.98 | 0.237 |
| 1.0 | 0.95 | 0.182 | 0.132 | 0.0226 | 5.95 | 1.05 | 119.8 | 105.4 | 0.224 | 2.94 | 0.182 |
| 0.5 | 0.95 | 0.161 | 0.116 | 0.0176 | 6.13 | 1.52 | 118.2 | 106.4 | 0.189 | 3.15 | 0.161 |
| 0.1 | 0.95 | 0.111 | 0.080 | 0.0078 | 6.54 | 2.43 | 114.9 | 108.3 | 0.110 | 3.51 | 0.111 |
| clean wing | | 0 | 0 | 0 | 7.475 | 3.5 | 108.2 | 108.2 | 0 | 3.5 | 0 |

described in Fink, et al. [19]. These values are $\alpha_c = 7.47$ and $T = 502.3$ lb. These values also correspond to the minimum drag to lift ratio of 0.101.

The next step is to derive a stall margin for a roughened aircraft that percentage-wise is the same as for takeoff with a clean aircraft. This was accomplished by applying the experimental wind tunnel results from Appendix III to the general aviation lift curve described by Fink as follows. A clean aircraft will take-off at a lift coefficient at a certain percentage less than the maximum clean lift coefficient in order to have an adequate stall margin. This also implies that the takeoff will occur at an angle of attack, $\alpha_c$, less than the stall angle. Consider that the lift coefficients for a roughened aircraft versus angle of attack was calculated by taking the clean aircraft (not the airfoil) lift coefficient at a clean angle of attack and reducing the lift coeffcient by the amount:

$$\Delta C_L = ( \Delta C_{Lm}/C_{Lm})C_L, \qquad (54)$$

and simultaneously reducing the angle of attack with respect to zero lift by the amount:

$$\Delta \alpha = ( \Delta \alpha_s / \alpha_s ) \alpha, \qquad (55)$$

which is proportional to $\Delta C_{Lm}/C_{Lm}$. We note the relative loss in airfoil lift $\Delta C_{Lm}/C_{Lm}$ given in Appendix III is a function of relative roughness height, $(k_s/c)$, percentage coverage of roughness, $P$, and the chord Reynolds number, $Re_c$, which allows application of the airfoil data to the aircraft and is transparent to aspect ratio effects. Thus to obtain the same adequate stall margin for a roughened aircraft, or at takeoff a lift coefficient at the same certain percentage (that is, 20%) below the roughened maximum lift coefficient, will also require a reduction in the clean takeoff angle of attack, by the ratio $\Delta \alpha_s / \alpha_s$ with respect to zero lift. We then get the angle of attack at takeoff for an adequate stall margin on a roughened aircraft as:

$$\alpha_R = (1 - \Delta\alpha/\alpha)(\alpha_C - \alpha_O) + \alpha_O \qquad (56)$$

where $\alpha_O$ is angle of attack at the aircraft's (not the airfoil's) zero lift (that is, $\alpha_O = -4.06$). Thus the input to Equations (52) and (53) used to evaluate a takeoff procedure modification are derived from the above analysis by requiring the same percentage stall margin as occurred with a normal clean wing takeoff.

The clean aircraft drag coefficient, $C_{D_C}$, for the general aviation aircraft as a function of $\alpha_C$ is obtained from Fink, et al. [19]. The roughened aircraft drag coeffcient, $C_{D_R}$, in Equation (53) is calculated from the clean drag curve as:

$$C_{D_R} = C_{D_C} + \Delta C_{D_C} + \Delta C_{D_1} = C_{D_C} + \Delta C_D \qquad (57)$$

where $\Delta C_{D_1}$ is the drag increment on the fuselage due to roughness and $\Delta C_{D_C}$ is the drag increment on the wing section due to roughness. Both $\Delta C_{D_1}$ and $\Delta C_{D_C}$ are given by empirical relationships in Appendix III. Table VIII shows the computed values of $\Delta C_L/C_L$, $\Delta\alpha/\alpha$, $\Delta C_D$, and $\alpha_R$ at takeoff for the different roughness heights 0.1, 0.5, and 1.0 mm and the relative coverage of 1.0 and 0.95 on the wing section. These values were used as input to Equations (52) and (53).

## 5.1  TAKEOFF PERFORMANCE EVALUATION

Galins and Shirkey's suggestion implied the roughened aircraft weight to be same as the clean aircraft weight, $W_R = W_C$. Equations (52) and (53) were solved for the climb angle $\gamma_R$ and the takeoff speed $V_R$ that sustain a steady climbing flight with an adequate stall margin. The results in Table VIII show that for roughness in which the loss is $\Delta C_L/C_L > 0.3$ the climb angle becomes negative and the takeoff speed is 1.2 that of the clean aircraft. To climb at all for $\Delta C_L/C_L > 0.3$, the stall margin will have to be reduced to an unsafe level. Weeks' suggestion implies the climb angle remain the same, $\gamma_R = \gamma_C$, and that

54

Equations (52) and (53) be solved for the increased takeoff speed, $V_R$, and the relative reduced takeoff weight $(W_c - W_R)/W_c$ that sustain a steady climbing flight with an adequate stall margin. The favorable results in Table VIII show that for different roughness conditions the takeoff speed, $V_R$, deviates from $V_c$ by about ±3%, and the relative reduction in the aircraft weight show somewhat the same trends as $\Delta C_L/C_L$. Although this is a feasible takeoff procedure modification, it is not the simplest approach operationally. Ljungstroem's suggestion of just partially cleaning the wings will result in an unsafe takeoff if the aircraft is loaded at the maximum clean gross weight, as is obvious from Table VIII. The final option, which is the author's suggestion, is to maintain the same takeoff speed, $V_R = V_c$, and solve for the climb angle, $\gamma_R$, and the relative aircraft weight reduction, $(W_c - W_R)/W_c$, from Equations (52) and (53) in order to sustain a steady climbing flight with an adequate stall margin. The results in Table VIII indicate that the climb angle $\gamma_R$ deviates not more than 0.5 degrees from $\gamma_c$ and the required relative aircraft weight reduction $(W_c - W_R)/W_c$ is practically the same as the relative lift loss, $\Delta C_L/C_L$. This means the maximum gross weight of the roughened aircraft can be approximated as:

$$W_{Rmax} \simeq (1 - \Delta C_L/C_L)\ W_{cmax} \qquad (58)$$

This takeoff procedure does not have to use explicitly the aircraft's equations of motion and is related to partial removal of frost through the relative lift loss term, $\Delta C_L/C_L$. Of course, while setting $V_R = V_c$ and maintaining constant airspeed during climbout, the angle of attack will naturally be at the reduced value for a safe margin above stall.

In this section we present the conceptual conclusions and in the last section of this report are the operational recommendations concerning aircraft takeoff. To summarize the results

obtained, the increase in takeoff speed is not always effective in compensating for the lift loss and the drag increment due to roughened wings. A maximum gross weight reduction, however, will always be effective. Thus the most probable cause of takeoff accidents with uniform roughened wings, with thrust maintained, and with normal takeoff procedures is the loading of an aircraft to its maximum allowable gross takeoff weight. Although one of the purposes of a safe stall margin is to tolerate small wing roughnesses, it is rather obvious the typical nocturnal frost thicknesses reported here and elsewhere can bring the stall margin down to an unsafe level (at least for the general aviation aircraft examined) when fully loaded. Being at an unsafe stall margin can lead to a loss of control in flight when the engine thrust is reduced, or when the proper takeoff rotation rate is exeeded, or when adequate air speed is not maintained. In this type of accident a successful climb is obtained, but a pilot not realizing his unsafe stall margin does a "normal" maneuver leading to a loss of control of his aircraft. In examining some NTSB records, it appears this is the most common type of takeoff accident with wing roughness. One example is the Cessna 180 fatal crash that occurred at the Berlin Municipal Airport in New Hampshire in 1977 [20]. The pilot failed to remove the ice and snow and took on two passengers. His climb was successful, and a normal power reduction after 1500 feet from departure was accomplished. Then he lost control and crashed. Another example is the crash of a Japan Air Lines McDonnell Douglas DC-8-62F at Anchorage, Alaska [21]. The NTSB report reads: "the conditions were favorable for the accretion of rime icing (or hoar frost) from the time the aircraft approached Anchorage until the crash." From the flight recorder data and simulation studies, they found the maximum lift coefficient had to be reduced about 15% and stall at an angle of attack 2 degrees less than normal for the recorded aircraft trajectory. This alone may not have prevented

continued flight, but "the aircraft may have been rotated to an excessive pitch angle just before it reached takeoff speed, and the stall stick shaker did not activate until near impact." Finally, "the probable cause of the accident was a stall that resulted from the pilot's control inputs aggravated by airframe icing while the pilot was under the influence of alcohol."

In the more severe cases, there is no stall margin available, and a pilot would be unaware of it until too late, thus leading to an accident. Such appears to be the case in the Air Florida Boeing 737 crash in a snowstorm at Washington D.C., Jan 13, 1982 [22]. Although wing roughness is due to snow/ice, not frost, the conclusions by NTSB are pertinent. There was no stall margin because "the aircraft's stall warning stick shaker activated almost immediately after liftoff and continued until impact." In summary, the aircraft actually had a lower thrust than the pilot thought it had and the flight crew apparently had only a limited experience with airframe icing and its effects on the aircraft. NTSB asserts that "the aircraft could not sustain flight because of the combined effects of airframe snow or ice contamination which degraded lift and increased drag and the lower than normal thrust set by the reference to the erroneous EPR indications. Either condition alone should not have prevented continued flight. Continuation of flight should have been possible immediately after stick shaker activation if appropriate pitch control had been used and maximum available thrust had been added. While the flight crew did add appropriate pitch control, it did not add thrust in time to prevent impact."

A further issue that should be addressed is what the lift and drag penalties were as determined from computer simulation and flight recorder data, or from a knowledge of wing ice/snow thickness as related to the aerodynamic penalties. This knowledge of the aerodynamic penalties is needed to compute

whether the flight was recoverable or not by application of maximum thrust.

Another issue is that if the pilot knew what his tolerable wing roughness for his particular gross weight for a safe stall margin was and was able to estimate the roughness height, then he would have aborted takeoff.

To confirm the above conceptual causes of the takeoff accidents and to test the practicality of the takeoff procedure modification, one could suggest three phases of testing. First, if necessary, is to re-evaluate the constants in the $\Delta C_{L_m}/C_{L_m}$ and $\Delta \alpha_s/\alpha_s$ empirical correlations for a specific wing configuration and a specific kind of roughness in a wind tunnel. Perhaps a simulator can investigate probabilities of a takeoff accident using the algebraic relationships of the type shown in Appendix III and using the different takeoff procedures suggested. Second, test flight an aircraft with the weight reduction takeoff procedure modification using the same kind of roughness and wing section. This phase is to test to see if the weight reduction takeoff procedure modification is sound for the highly controlled wing roughness. Thirdly, take the same aircraft with cleaned wings and expose it to the nocturnal frost formation. Measure its thickness, percentage coverage, and uniformity of coverage. Then, based upon the previous analysis, determine the maximum gross weight of the roughened aircraft to assure a safe takeoff margin. Finally, takeoff with the aircraft and compare its observed performance to that predicted for the observed roughness.

# SECTION 6

## PREDICTING OR FORECASTING NOCTURNAL FROST RESULTS

The nocturnal frost formation model can be run with two modes to assess frost growth and aerodynamic penalties. The first is the diagnostic mode which uses the observed atmospheric profiles such as those in Tables I to VII. Figure 12 is the result using the data from Table I at the end of the run. The graph shows a wing section temperature and frost density and thickness distributions on the NACA 64A215 section at the end of the run at 5 A.M. Likewise, Figure 13 corresponds to the data input from Table V, and Figure 14 corresponds to the data input from Table VI with the predicted temperatures, frost density and thickness at the end of the run. Generally speaking, the frost on the underside of the wing section has a high frost density but a very low frost thickness. The frost on the topside has the frost density decrease in the same rate as the mass transfer coefficient, but the frost thickness tends to stay at a high value. Finally, the ripple effect in the wing section temperatures is a reflection of the spar support structures in the wing section.

When Equation (A3.9) in Appendix III is set equal to zero, P, the percentage roughness coverage from the leading edge, equal to one, the value of $Re\left(\dfrac{k_s}{c}\right)$ at which the aerodynamic penalty begins to appear is about 0.73. On the other hand, it is recalled that on a flat plate the admissible frost thickness roughness effect is, $Re\left(\dfrac{k_s}{c}\right) = 100$, according to Biguria and Wenzel [11]. The pressure gradient on the wing section, in conjunction with the roughness effect, may have effectively reduced the admissible frost thickness by an order of magnitude. Thus to determine the value for P, a conservative approach was taken. That is, starting from the leading edge, and moving back, the first frost

Figure 12. End of the Run Time Wing Section Surface Temperature, Frost
Density and Thickness versus Relative Chord Location
Corresponding to Table I Input Data in the Diagnostic Mode.

Figure 13.  End of the Run Time Wing Section Surface Temperature, Frost
Density and Thickness versus Relative Chord Location
Corresponding to Table V Input Data in the Diagnostic Mode.
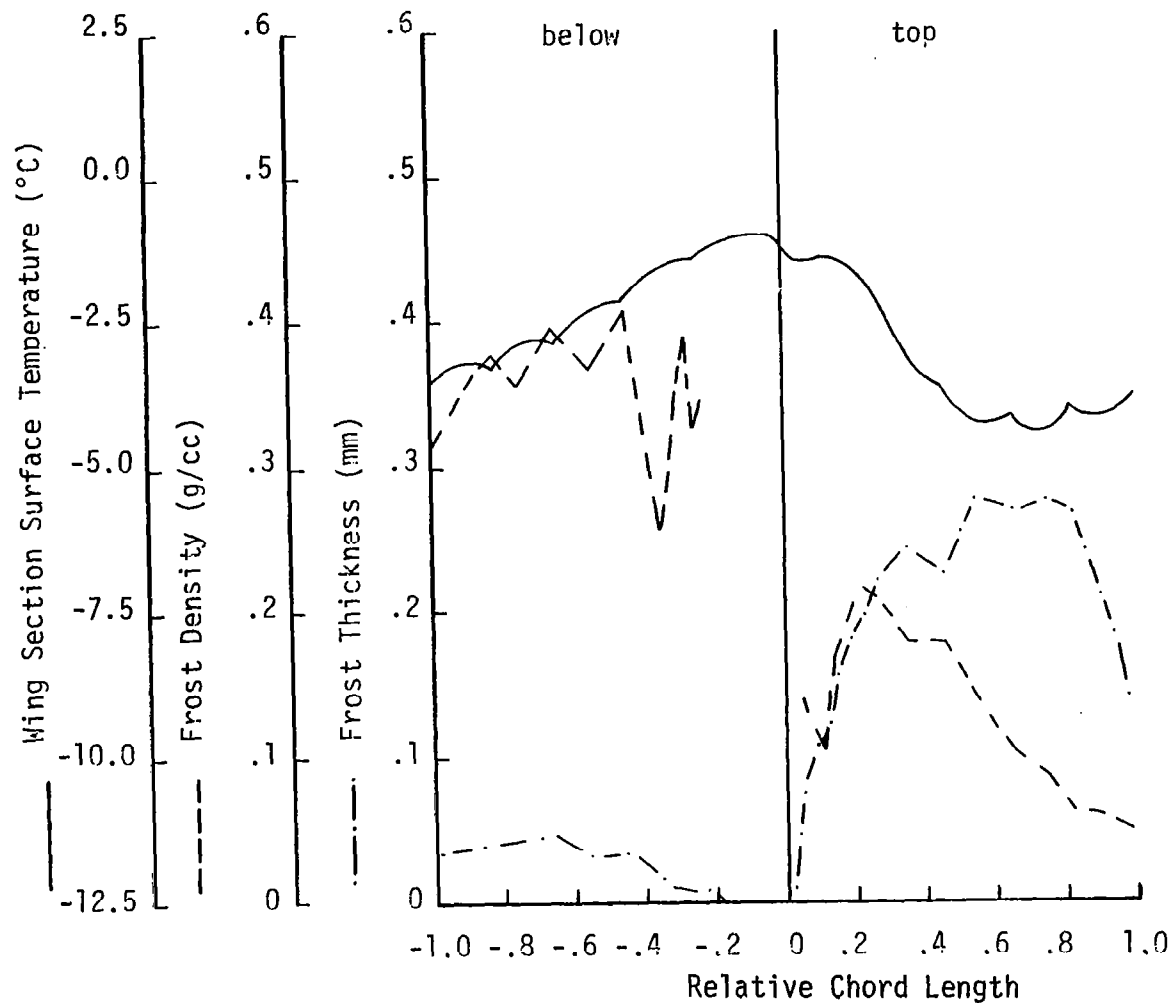
Figure 14. End of the Run Time Wing Section Surface Temperature, Frost Density and Thickness versus Relative Chord Location Corresponding to Table VI Input Data in the Diagnostic Mode.
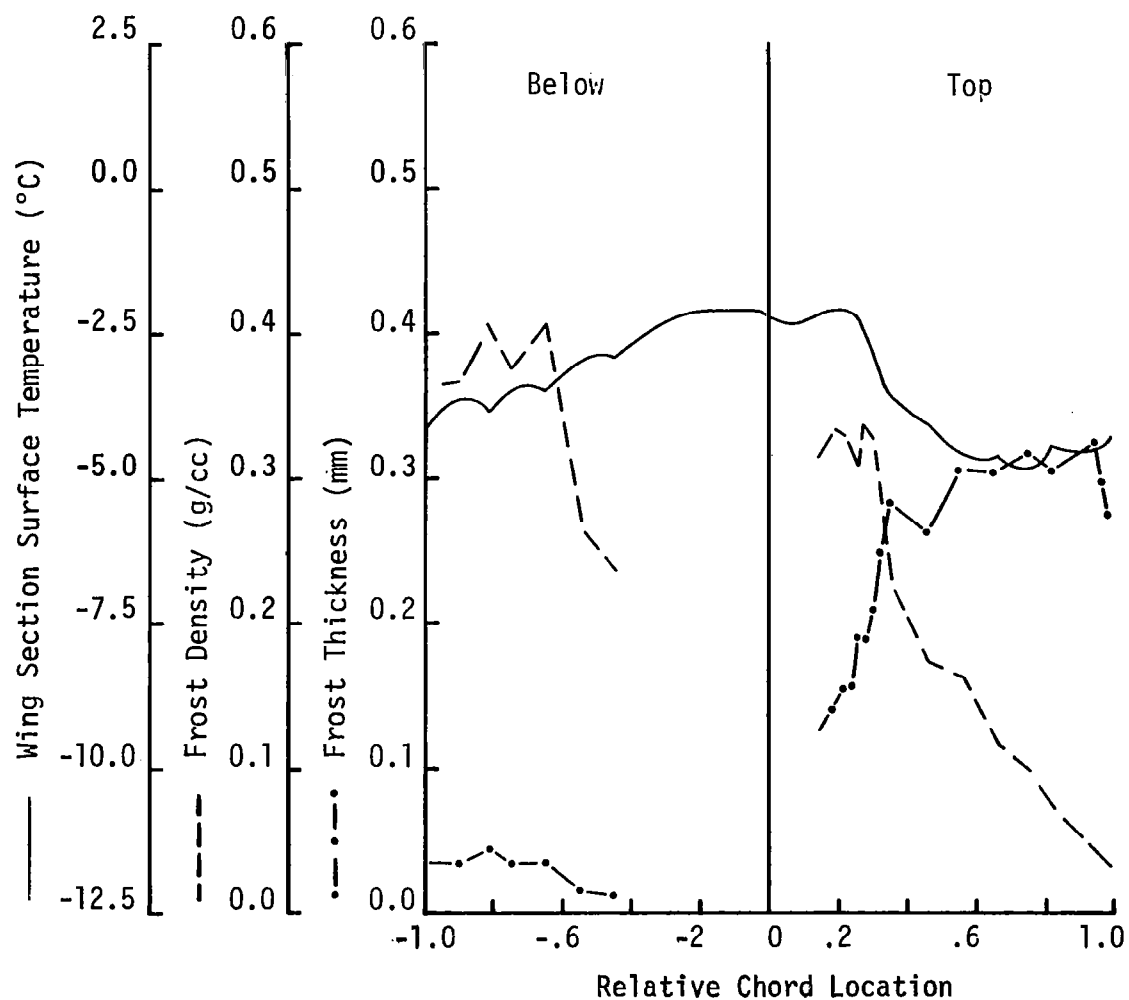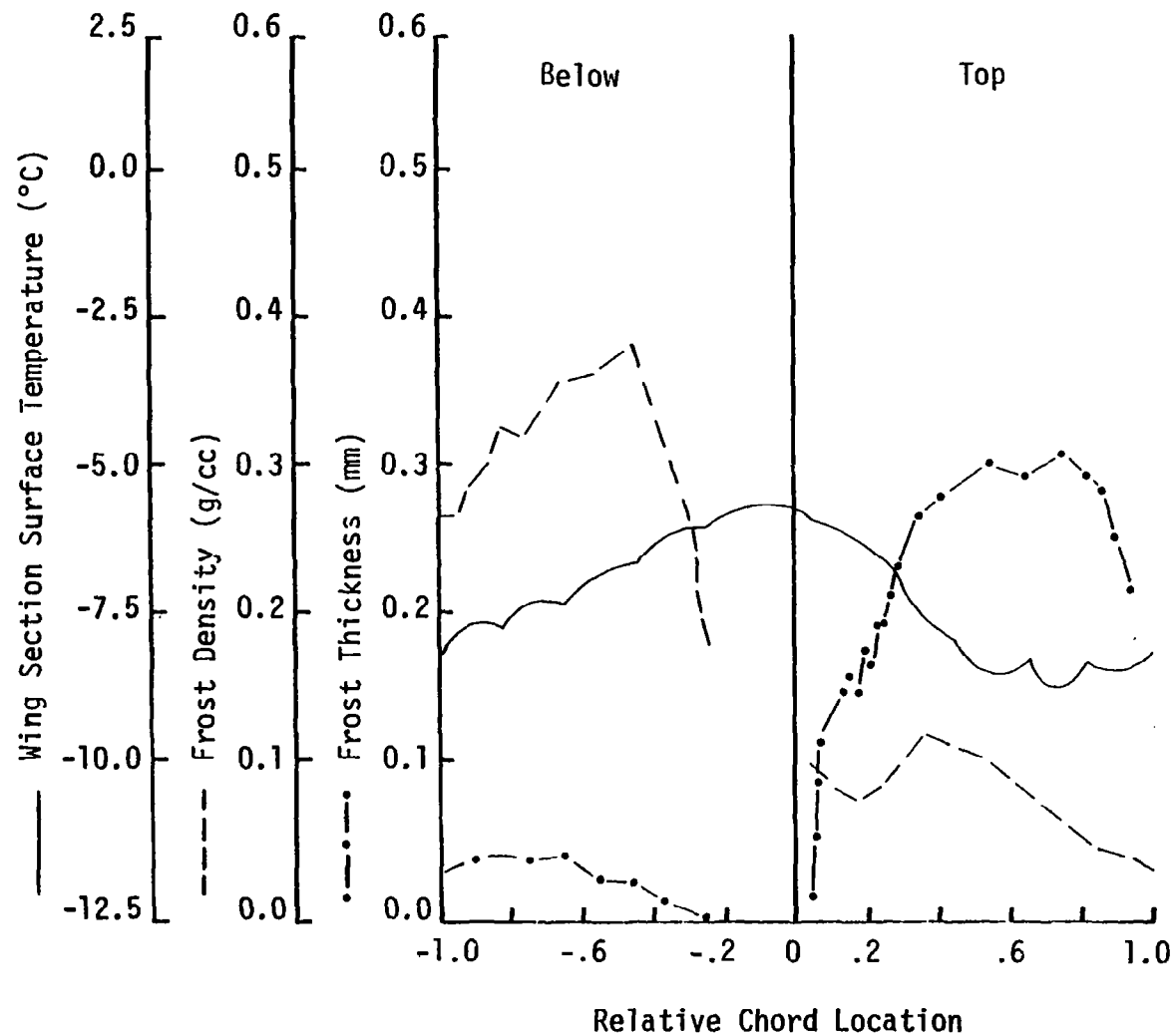
thickness that has $\text{Re}\left(\dfrac{k_s}{c}\right) \geq 0.73$, will determine P, and then the rest of frost on the way back to the trailing edge will be used to compute an average frost thickness.

The averaged frost thickness, P, and a takeoff velocity at 108 ft/sec is used as an input to Equations (A3.4) to (A3.10) in Appendix III to determine the drag and lift penalty. Using this approach, the percentage maximum lift coefficient lost for the Figure 12, frost thickness distribution, is calculated as 16%. From the frost thickness distributions as shown in Figure 13, the percentage maximum lift loss is 10%; and from the frost thickness distributions shown in Figure 14, the percentage maximum lift loss is 15%.

The second mode of the nocturnal frost formation is the forecasting of frost at 6 A.M. using the atmospheric data measured at 5 P.M. The atmospheric profile is forecasted as follows. The pressure, wind speed, and cloud cover are held constant throughout the night. The absolute humidity is held constant until the air temperature reaches the dew-point temperature, then the absolute humidity is set equal to the saturated absolute humidity at air temperature. The dry air temperature profile is forecasted as:

$$T_a = \frac{T_o + T_M}{2} + \frac{T_o - T_M}{2}\sin\left(\frac{2\pi(t + 11)}{32}\right) \tag{59}$$

$$T_o = \frac{2T_{5pm} - 0.16853T_M}{1.83147} \tag{60}$$

$$T_M = T_{5pm} - \left[t_{6am} - \left(\frac{T_{5pm} - T_{d_{5pm}}}{2}\right)\right]\left[1 - K_N\right] \tag{61}$$

taken from Bagdonas, et al. [6]. When the air temperature reaches the dew-point, fog or rain is assumed to form. Then the air temperature is treated as a constant when it reaches a condensation temperature given by:

63

$$T_{condense} = \text{minimum} \left( T_{d_{5pm}}, \quad \frac{2}{3}T_{d_{5pm}} + \frac{98 - \phi_a}{12} \right) \quad (62)$$

in degrees Celsius.

Figure 15 shows the results at the end of a forecasted nocturnal frost formation run. The input data is summarized in the figure. Plotted are frost density and thickness distributions on the wing section. Also included in the figure are the lift and drag penalties. Figures 16 and 17 show the similar types of information for other atmospheric conditions at 5 P.M. and forecasted throughout the night until 6 A.M. Figure 17 shows how the sun dissipates completely the nocturnal frost, in this case, after one and a half hours. By making several more runs for the various meteorological profiles, the averaged frost thickness at 6 A.M. can be plotted as a function of air temperature, relative humidity, wind speed, emissivity, cloud cover, and wind direction. In Figure 18 are plotted averaged frost thickness versus temperature. The wind is from behind the wing in each case, the emissivity is 0.2, and the night is clear. The averaged frost thickness shows only minor variation with wind, but shows strong increases with relative humidity and temperature increase. One can draw somewhat similar conclusions for Figure 19 for an emissivity of 0.85 (corresponding to a painted surface). We note the frost thickness can grow as thick as about 1mm, although a thickness of 0.5mm is more common. Also shown in Figures 18 and 19 are the regimes of condensation only and the regime of frost/ice growth. The greatest frost thicknesses occur at air temperatures of 2.5°C to 5°C, relative humidity of 100%, during calm and clear nights. In Figure 18 is shown the open diamond symbol corresponding to 50% cloud (cumulus) cover, 70% relative humidity, calm winds of 0.5 m/s, and an air temperature of 0°C. The frost thickness was about one-third of that of the clear night with other conditions the same. In general, wind speeds less than 0.5 m/s were clearly in the mixed convection regime, but the frost thickness tends to be the same as at 0.5 m/s.

Wing Section Surface Temperature (°C): 2.5, 0.0, -2.5, -5.0, -7.5, -10.0, -12.5

Frost Density (g/cc): 0.6, 0.5, 0.4, 0.3, 0.2, 0.1, 0

Frost Thickness (mm): 0.6, 0.5, 0.4, 0.3, 0.2, 0.1, 0

Below

Top

5 P.M. Data:

Wind Speed = 0.5 m/s
Cloud Cover = 0.0 m/s
Air Temperature = 0°C
Relative Humidity = 50%

| Curve Number | Chord (meters) | Takeoff Speed (m/s) | $\frac{\Delta C_L}{C_L}$ | $\frac{\Delta \alpha}{\alpha}$ | $\Delta C_D$ |
|---|---|---|---|---|---|
| 1 | 1.50 | 33 | 0.212 | 0.154 | 0.0125 |
| 2 | 3.32 | 75 | 0.315 | 0.228 | 0.0045 |

-1.0 -.8 -.6 -.4 -.2 0 .2 .4 .6 .8 1.0

Relative Chord Location

Figure 15.  A Sample of Nocturnal Frost Forecasting and the Corresponding
Aerodynamic Penalties, on a NACA 64A215 Wing Section with
20° Flaps at 6:00AM.

below        top

5 P.M. data:      6 A.M. penalties:

wind speed=5 m/s
cloud cover=0.0
air temperature=-10°c
relative humidity=50%

$\Delta C_{L} / C_{L}$ = .277

$\Delta\alpha/\alpha$ = .201

$\Delta C_{D}$ = .0119

Wing Section Surface Temperature (°C): 2.5, 0.0, -2.5, -5.0, -7.5, -10.0, -12.5

Frost Density (g/cc): .6, .5, .4, .3, .2, .2, 0

Frost Thickness (mm): .6, .5, .4, .3, .2, .2, 0

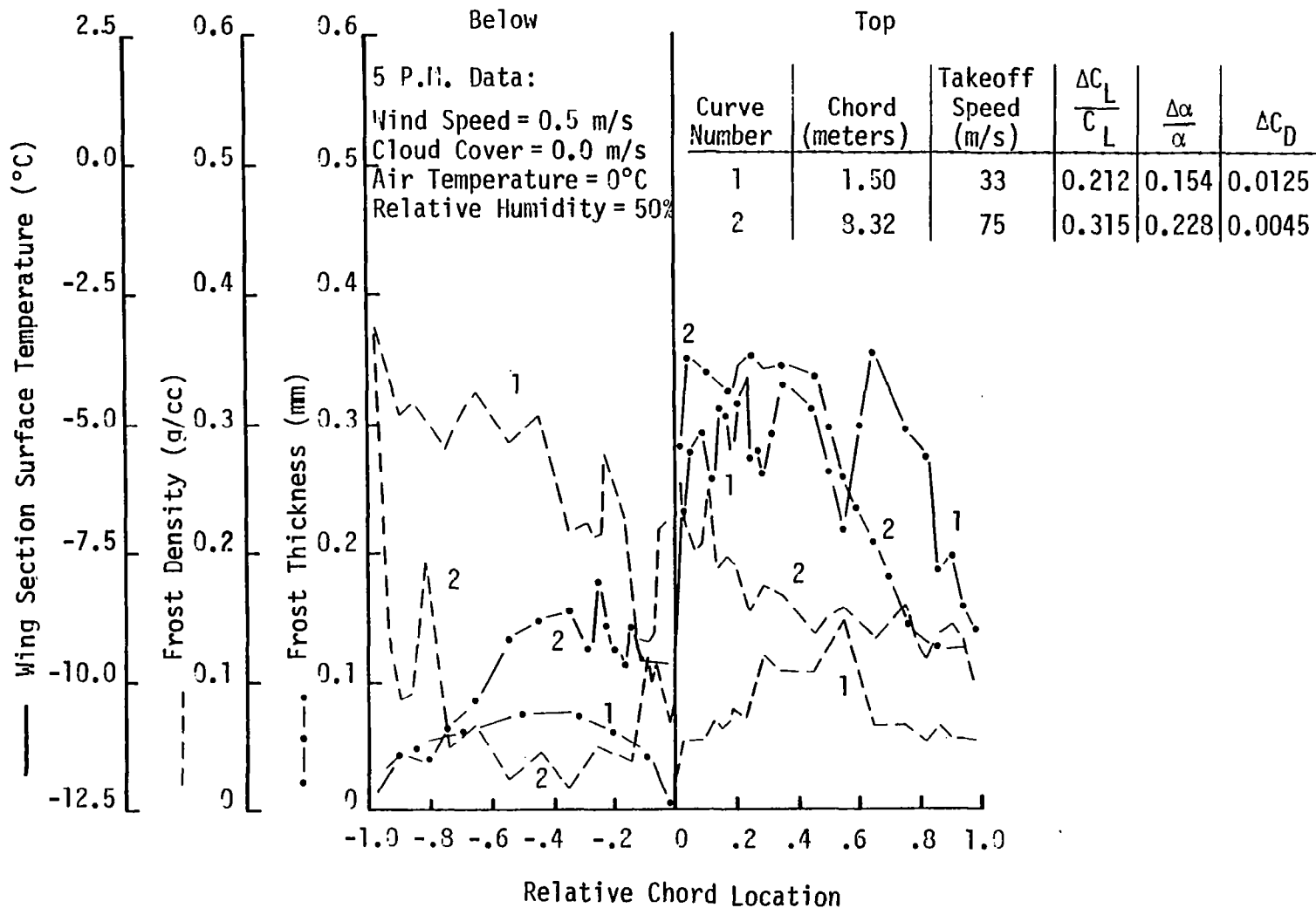Relative Chord Location: -1.0 -.8 -.6 -.4 -.2 0 .2 .4 .6 .8 .10
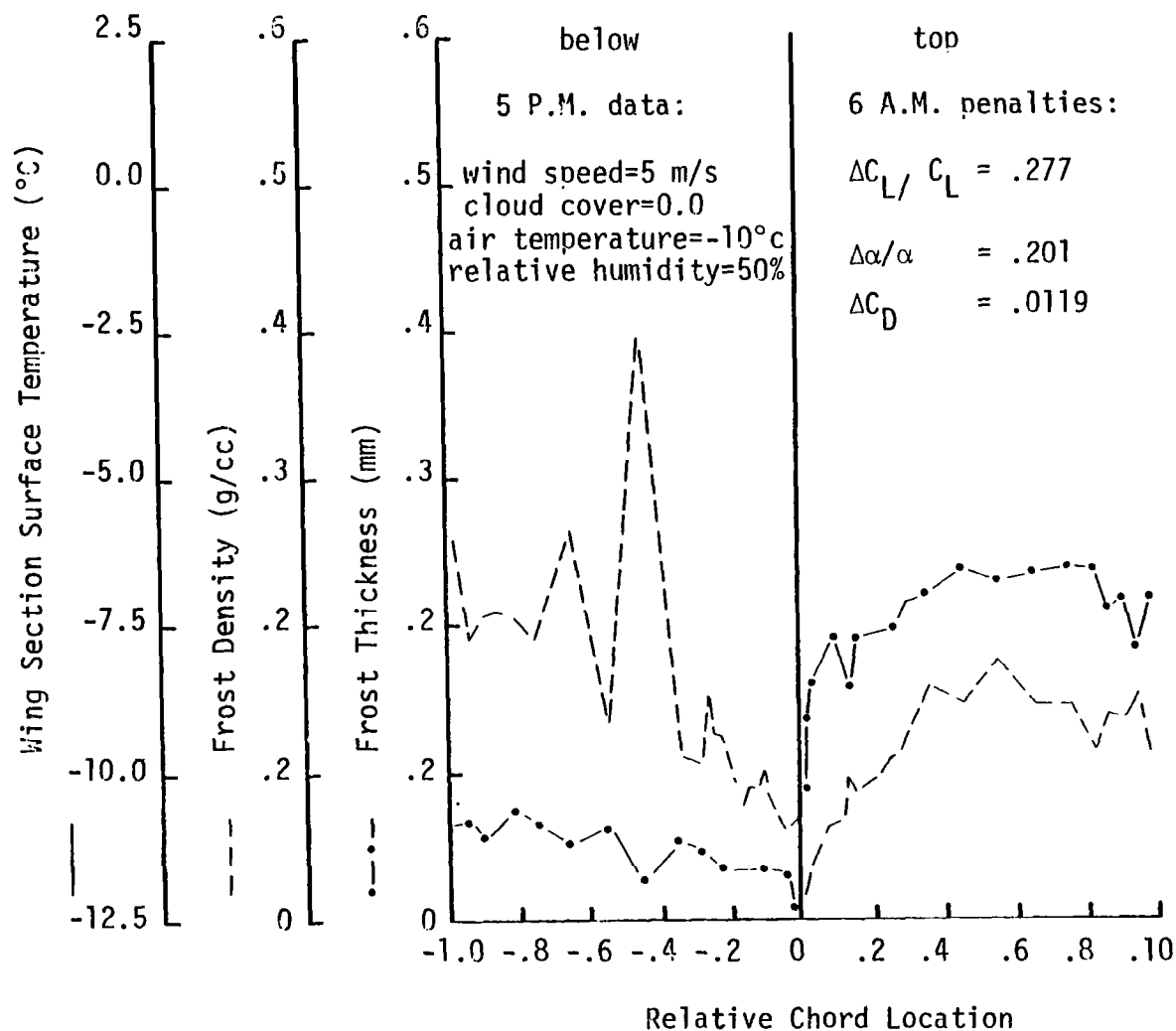
Figure 16. A Sample of Nocturnal Frost Forecasting and the Corresponding Aerodynamic Penalties on a NACA 65A215 Wing Section with 20° Flaps at 6:00AM

Wing Section Surface Temperature (°C)

2.5
0.0
-2.5
-5.0
-7.5
-10.0
-12.5

Frost Density (g/cc)

0.6
0.5
0.4
0.3
0.2
0.1
0.0

Frost Thickness (mm)

0.6
0.5
0.4
0.3
0.2
0.1
0.0

Below                    Top

At 5 P.M.

Air Temperature = 0°C
Relative Humidity = 50%
Wind Speed = 0.5 m/s
Cloud Cover = 0.0

6A.M.
7A.M.
6A.M.
7A.M.
6A.M.
6A.M.
7A.M.
7A.M.

-1.0    -.6    -.2    0    .2    .6    1.0

Relative Chord Location

Figure 17.  An Example of Forecasting Nocturnal Frost Formation and of
Frost Dissipation Due to the 6:00AM Sunrise.  The Frost is
Completely Melted/Evaporated by 7:30AM or After 1-1/2 Hours
of Sun Flux.

Figure 18. Forecasted Averaged Frost Thickness on Top of
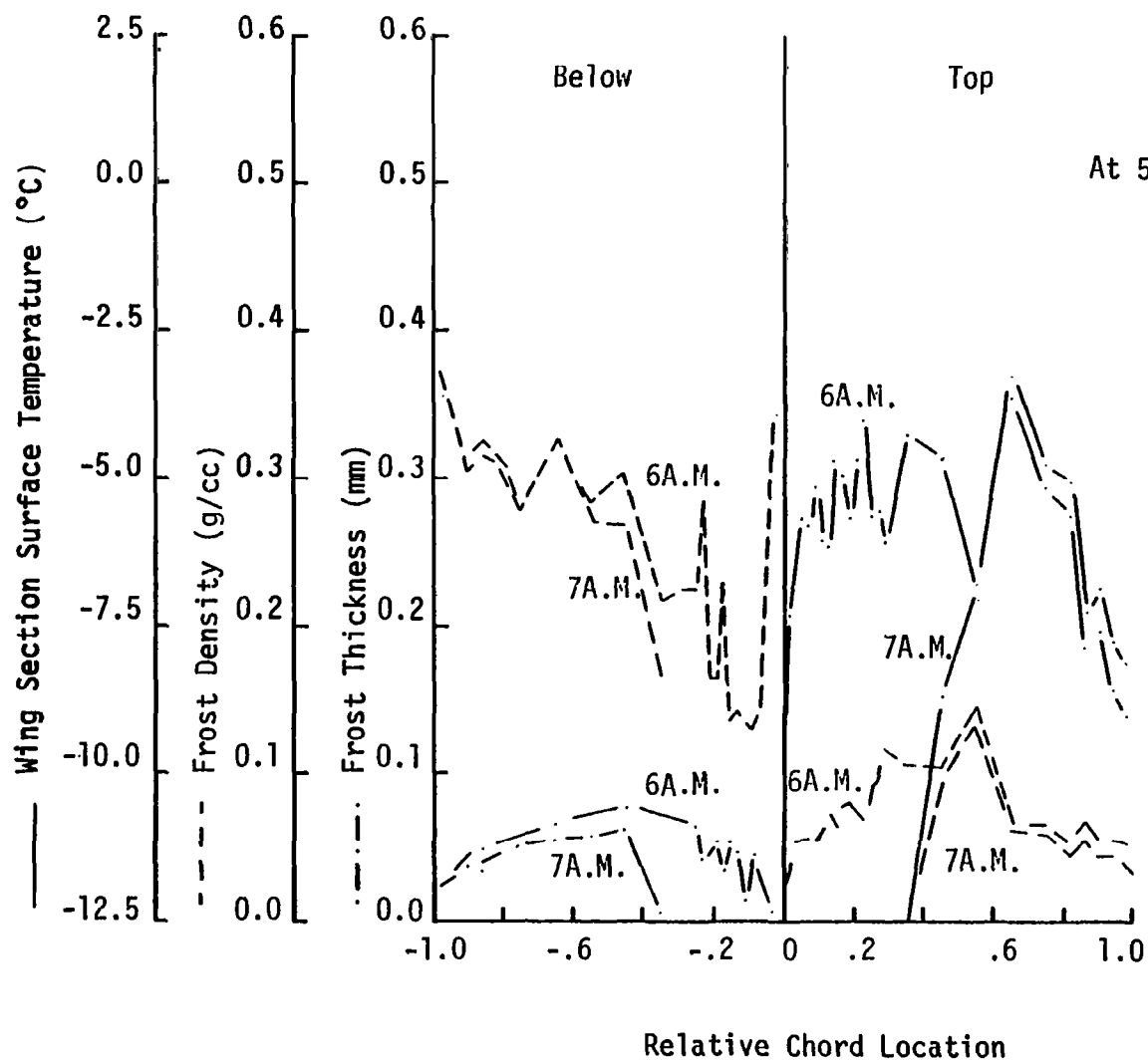Wing Section at 6:00AM for Surface Emissivity
of 0.20 Versus Air Temperature, Relative
Humidity, and Wind Speed at 5:00PM.
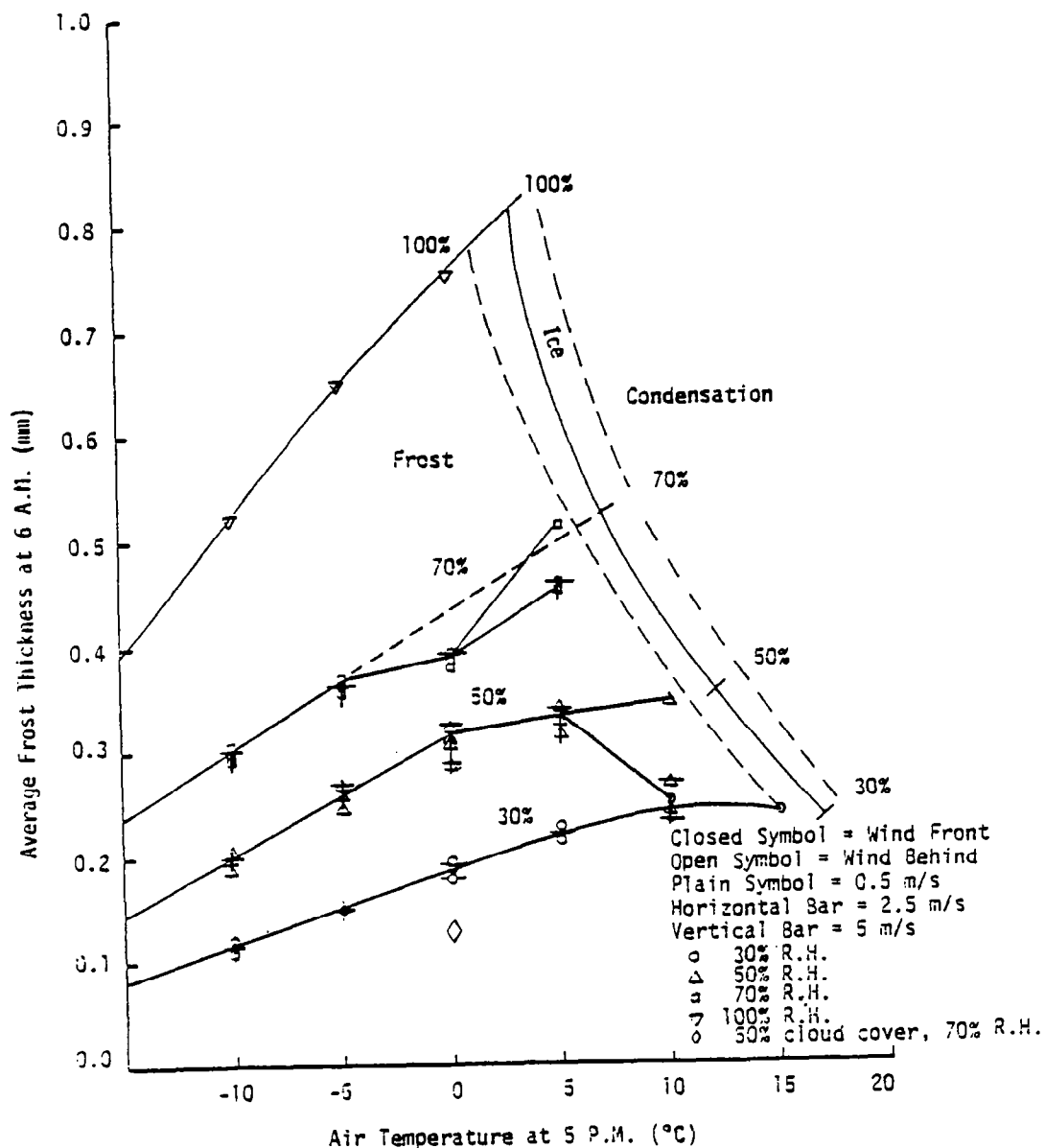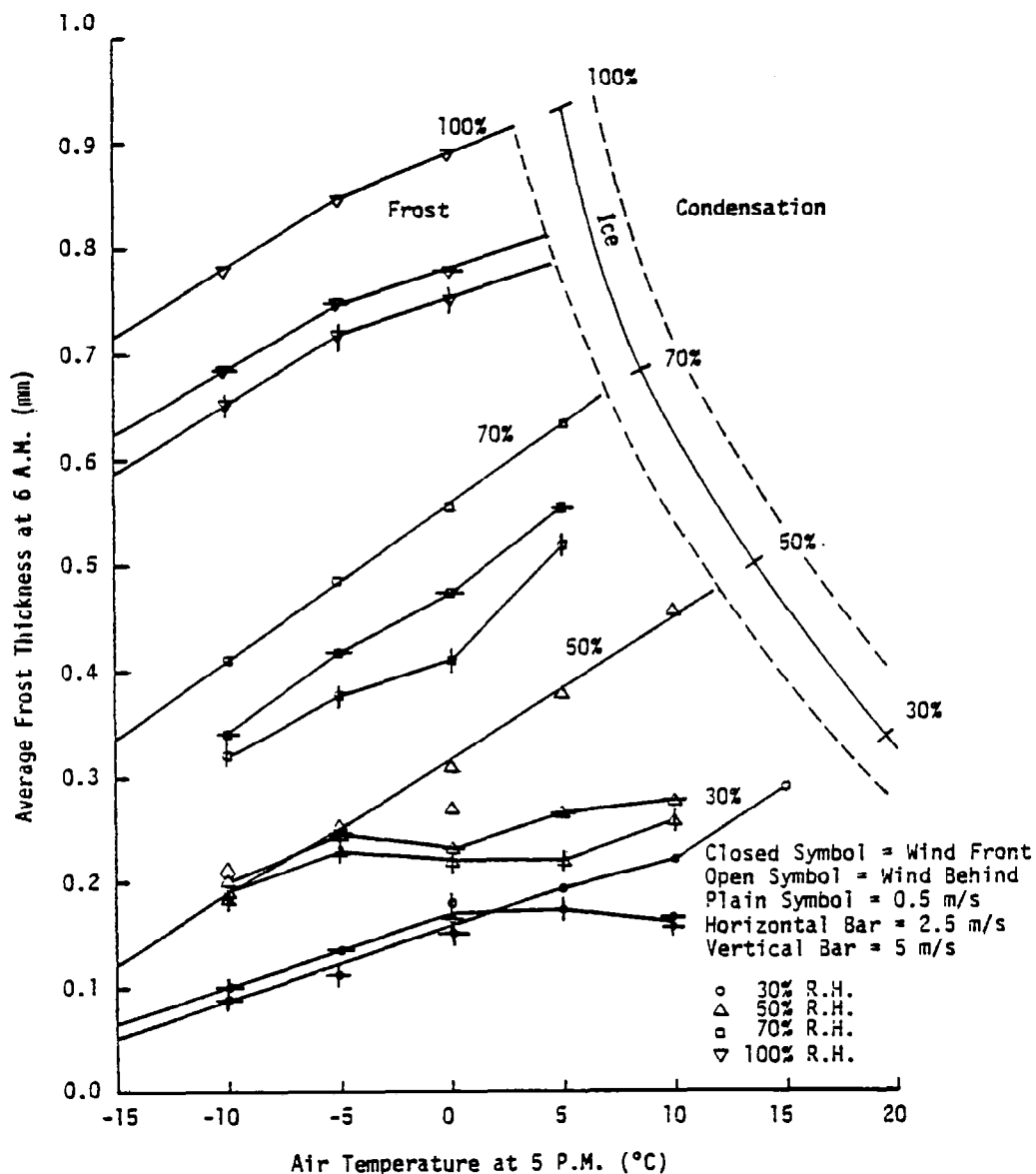
Figure 19.   Forecasted Averaged Frost Thickness on Top
of Wing Section at 6:00AM for Surface Emissivity
of .85 versus Air Temperature, Relative Humidity,
and Wind Speed at 5:00PM.

# SECTION 7

## CONCLUSION

The research on the nocturnal frost formation on a wing section was undertaken to better explain the hazard associated with frost on a wing section during a takeoff. This paper has provided some pertinent information. A nocturnal frost formation model on a wing section has been developed that predicts when the nocturnal frost will form and also its thickness and density as a function of time. The model shows satisfactory comparison with the experimental data on a flat plate. An analysis of the aerodynamic penalties as related to the nocturnal frost formation properties was made to determine how much the takeoff performance would be degraded by a specific frost layer. With an aircraft takeoff assuming equations representing a steady climbing flight, it was determined a reduction in the maximum gross weight or a partial frost clearance and a reduction in the takeoff angle of attack are needed to neutralize drag and lift penalties. This, in turn, was related to the nocturnal frost layer. A sensitivity study was performed to determine the atmospheric conditions which produce the most hazardous frost buildup.

Under calm conditions, at 100% relative humidity, 5°C air temperature, and clear skies, the frost thickness got as high as 1 mm. On the average, the thicknesses were about 0.5 mm. These were the same magnitude of frost thicknesses reported by Weeks [4]. For a general aviation aircraft with a takeoff speed of 33 m/s, this gives a $Re(k_s/c)$ ranging from 1204 to 2409. From Figure 20, this corresponds to a 33% maximum lift loss, from which according to Equation (56) a pilot probably could not make a corresponding gross weight reduction. A 20% partial frost clearance will only require about a 10% reduction in maximum gross weight for a safe takeoff. Using Equations (56) and (58)
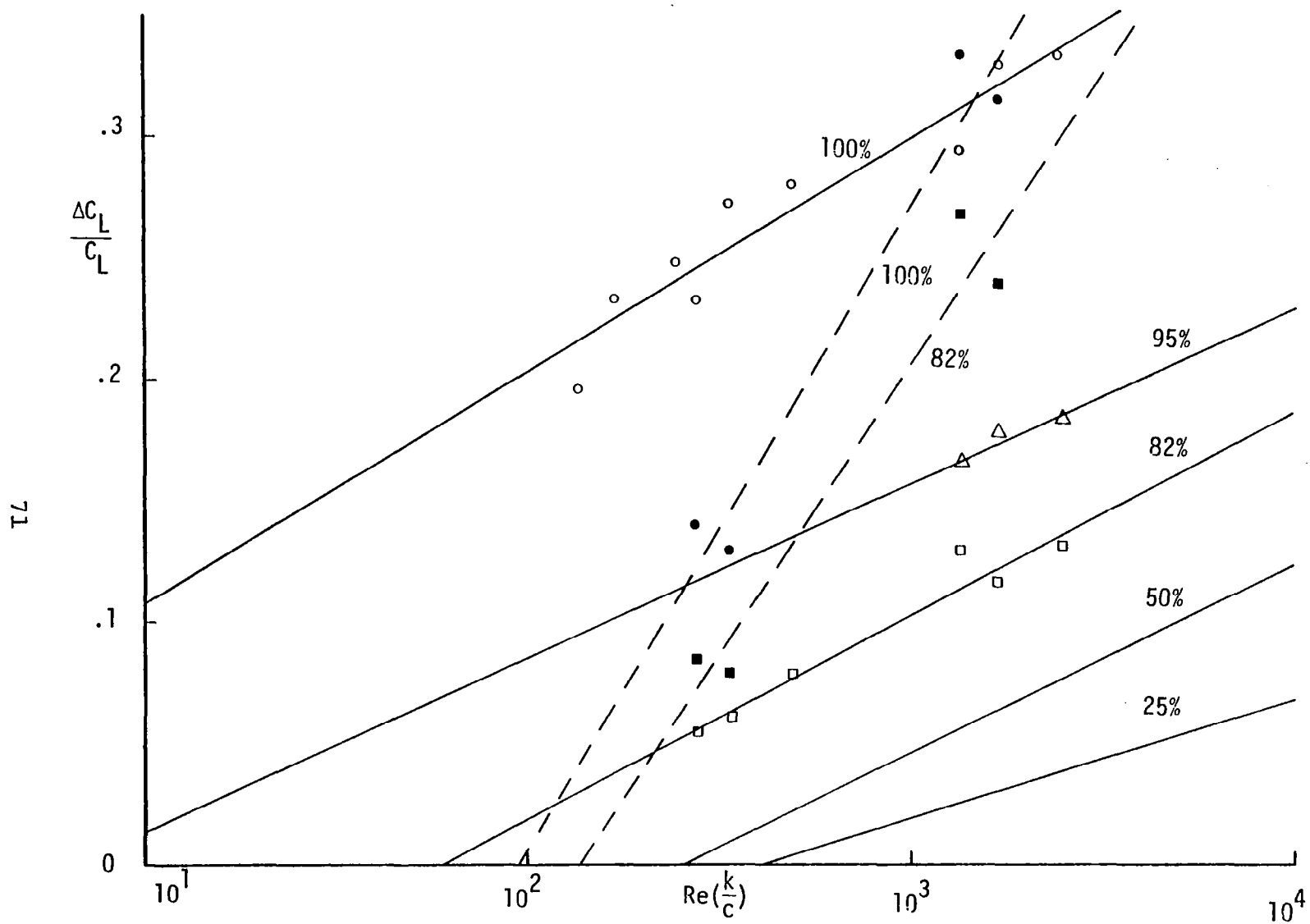
Figure 20. Relative Lift Loss of the NACA 65A215 Airfoil with 20° Flaps (and 25° Slats) versus Surface Roughness Distribution.

along with the empirical relationship in Appendix III, one can evaluate other tradeoff options between partial wing cleaning and the maximum gross weight reduction.

The increase in the takeoff speed was found to be ineffective in neutralizing the drag and lift penalties. As a result, it was determined that the most probable cause of takeoff accidents with uniform roughened wings was an aircraft fully loaded resulting in unsafe stall margins. The tradeoff performance analysis can be applied to most other aircraft, including transports, provided the relative lift loss $\Delta C_{L_m}/C_{L_m}$ and the relative angle-of-attack reduction $\Delta \alpha_s / \alpha_s$ can be properly related to $(k_s/c)$, P, and $Re_c$ of a particular aircraft. The drag increment due to roughness is only important as to how long it takes to reach takeoff speed and to show that an increase in takeoff speed was ineffective. Obviously, a wind tunnel and flight testing program would need to be conducted to verify the takeoff procedure modification before even considering operational application.

One type of operational application would be to automatically prevent an inexperienced or an incapacitated pilot from taxiing the aircraft if he exceeded his gross weight allowance. Also, existing stall warning systems should be modified to take into account the occurrence of maximum lift at a reduced angle of attack. Of course these applications imply automated measurements of $k_s$ and P, and other parameters which is an unlikely near term prospect.

Finally, Figures 18 and 19 show the forecasting of the regime of condensation only and the regime of frost/ice growth. One could conceivably use these figures to decide on preventive measures such as putting the aircraft in the hangar, covering the wings during the night with plastic sheets, waiting for the sun to dissipate the frost, or cancelling the flight plan. At the

At the present, as far as nocturnal frost is concerned, it is much more sane and convenient to take the preventive measures than to plan a takeoff with frost on the wings and control surfaces.

# APPENDIX I

## CALCULATION OF LONG WAVE LENGTH EMISSIVITY AND SOLAR ABSORPTIVITY

Expressions for the emissivity and solar absorptivity of the wing surface have been developed to account for the presence of ice and frost.

The emissivity for an ice layer is calculated using a simple radiative transfer model. The assumptions are that no radiation scattering occurs within the ice, and the ice layer is uniform in temperature. Radiation is assumed to originate from the plate as if no ice layer were present. This radiation is attenuated in traversing the ice due to absorption. Thus the net radiation from the wing transmitted through the ice layer is:

$$\sigma \varepsilon_s T_s^4 e^{-\psi x} \qquad (A1.1)$$

where $\psi$ is the attenuation coefficient (assumed to be independent of wavelength). In addition, each layer of ice of thickness, $dz$, is assumed to radiate as a gray body. This contribution to the radiation leaving the upper surface is:

$$(1 - R) \int_0^x \sigma(\psi\, dz) T^4 e^{-\psi(x-z)} \qquad (A1.2)$$

where $\psi\, dz = d\varepsilon$ is the emissivity of the layer $dz$ by use of Kirchoff's law and $R$ is the reflectance at the air-ice interface. The sum of Equations (A1.1) and (A1.2) is the total radiation flux leaving the upper ice surface, and this is equivalent to the radiation from a single interface having an emissivity $\varepsilon$ or:

$$q_{RAD} = \sigma \varepsilon T^4 = \sigma \varepsilon_s T^4 e^{-\psi x} + \sigma T^4 (1 - e^{-\psi x})(1-R) \qquad . \;(A1.3)$$

Furthermore, $(1 - R)$ is the emissivity of an infinitely thick ice layer through Kirchoff's law and is set equal to 0.94 in the model. The value for $\psi$ has been chosen as $10^5 m^{-1}$ [23, 24]. The final form of the surface emissivity is found from Equation (A1.3) as:

$$\varepsilon = ( \varepsilon_s - 0.94)\exp(-10^5 x) + 0.94 \quad . \qquad \text{(A1.4)}$$

The form of the expression for solar absorptivity is identical to Equation (A1.4) by use of Kirchoff's law. The solar absorptivity of the surface is given by:

$$\alpha = ( \alpha_s - 0.98)\exp(-10x) + 0.98 \quad . \qquad \text{(A1.5)}$$

For frost, the analysis is more complex because radiation scattering can occur, especially at solar wavelengths, and because the temperature within the frost layer cannot, in general, be considered uniform. The fact that frost is less dense than ice implies that less absorption should occur for frost than for bulk ice. On the other hand, considerably more scattering occurs in frost because of the inhomogeneities in refractive index caused by its porous structure. This scattering results in an increase in path length for radiation propagating through the frost layer and a resultant increase in absorption. These two effects tend to oppose each other and it is not unreasonable to expect both the long wave emissivity and solar absorptivity resulting from a thin frost layer to be similar to that resulting from an ice layer of the same thickness.

In the model, Equations (A1.4) and (A1.5) are used to determine the emissivity resulting from a thin ice layer on the plate surface. In case of frost, these expressions are modified to take into account the frost porosity. The modified expressions are also used when frost forms over ice. In the latter case, the thickness x is the total thickness (ice plus frost).

# APPENDIX II

## LAMINAR AND TURBULENT NATURAL CONVECTION ON
## AN INCLINED PLATE

The Sherwood and Nusselt numbers for Natural Convection are reproduced from Dietenberger [5] as modified for an inclined plate:

$$Sh_H = \frac{h_M H}{\rho_a D} = \eta(1+\omega_s), \quad Nu_H = \frac{h_H H}{k_a} = \eta/\xi, \quad (A2.1),(A2.2)$$

where:

$$\eta = 2\sqrt{Sc \cdot \Phi} \left[ \frac{Gr_H}{240\left(\frac{20}{21} + Sc\,\Phi\right)} \right]^{1/4}, \quad (A2.3)$$

$$Gr_H = \frac{gH^3}{\nu^2} \left[ \frac{\xi\,(T_a - T_s)}{T_a} + \frac{(\omega_a - \omega_s\,\Phi)}{(1.6453 + 2.6453\,\omega_a)} \right], \quad (A2.4)$$

$$\xi = \sqrt{\Phi^2 + 2\frac{Sc}{Pr}\,\Phi + 1} - \Phi, \quad (A2.5)$$

$$\Phi = \frac{1 + \omega_a}{1 + \omega_s}. \quad (A2.6)$$

The mean Nusselt and Sherwood numbers are:

$$\overline{Nu}_H = \frac{4}{3}Nu_H, \quad \overline{Sh}_H = \frac{4}{3}Sh_H. \quad (A2.7),(A2.8)$$

$Nu_H$ and $Sh_H$ for turbulent flow are:

$$Sh_H = 0.029791\ Sc^{7/15}\ \Phi^{1/5} \left[ \frac{Gr_H}{1+0.49426\ \Phi Sc^{2/3}} \right]^{2/5}, \quad (A2.9)$$

$$Nu_H = Sh_H \left(\frac{Pr}{Sc}\right)^{1/3}, \quad (A2.10)$$

$$\xi = 1.875 - \sqrt{0.765625 + 4.08973 \; \varphi \; [1 - \left(\frac{Sc}{Pr}\right)^{2/3}]} \quad .(A2.11)$$

The mean Nusselt and Sherwood numbers are:

$$\overline{Sh}_H = \frac{5}{6} Sh_H \; , \qquad \overline{Nu}_H = \frac{5}{6} Nu_H \qquad (A2.12),(A2.13)$$

## EMPIRICAL RELATIONSHIPS FOR THE DRAG, LIFT, AND ANGLE OF ATTACK PENALTIES

To evaluate the minimum drag coefficient of a streamlined fuselage covered with roughness at takeoff speed, we note the fuselage Reynold's number is usually in the tens of millions for a typical general aviation aircraft. It is assumed the fuselage is nearly all friction drag and treated by a flat plate model. For a smooth flat plate the local friction coefficient from the Handbook of Heat Transfer [7] is correlated as:

$$C_{f_S}/2 = 0.0131 \ Re_S^{-1/7} \qquad \text{for } Re_S \geqslant 10^7. \qquad (A3.1)$$

From Young [25], the correlation of the local friction coefficient over a fully rough flat plate is approximated by:

$$C_{f_R} = 0.0139 \ (k_S/s)^{1/7} \quad \text{for } 4 \times 10^{-7} < k_S/s < 5 \times 10^{-4}. \qquad (A3.2)$$

If P is the fraction of the plate roughened from the trailing edge, the relative drag coefficient increase of the plate is modeled by integrating Equations (A3.1) and (A3.2) in the expression:

$$\frac{\Delta C_{D_\ell}}{C_{D_\ell}} = \frac{\int_0^{(1-P)\ell} C_{f_S} \ ds + \int_{(1-P)\ell}^{\ell} C_{f_R} \ ds}{\int_0^{\ell} C_{f_S} \ ds} - 1. \qquad (A3.3)$$

The result is:

$$\frac{\Delta C_{D_\ell}}{C_{D_\ell}} = \left\lfloor \frac{1.06}{2} \left( Re_\ell \ \frac{k_S}{\ell} \right)^{1/7} - 1 \right\rfloor \left[ 1 - (1 - P)^{6/7} \right\rfloor \qquad (A3.4)$$

This equation predicts well the Hoerner's [26] very limited data on the minimum fuselage drag due to fully-covered roughness. Since Equation (A3.4) was not fitted to any aircraft data, it has some physical significance in that extrapolation is allowed beyond Hoerner's data but must remain within the range given by

Equations A3.1 and A3.2. Significant nocturnal frost is expected to occur only on the upper half of the fuselage. Thus Equation A3.4 was halved to estimate the drag increment, $\Delta C_{D_\ell}$, in Table VIII for the given values of $k_s$, and P was set to one. The average frost roughness height, $k_s$, on the fuselage was assumed to be same as that on the wing.

For a plain wing section fully covered with roughness at the Reynold's number in the millions, Hoerner's [26] shows a correlation of the airfoil minimum drag coefficient versus the variable, $k_s/c$, which is the same correlation for a flat plate multiplied by a constant. The constant is modeled as a function of the airfoil's thickness ratio, and at the 15% thickness ratio for the NACA 64 and 65 series airfoil, it shows the minimum drag coefficient is nearly all friction drag. Young [25] approximated the drag coefficient of a flat plate due to roughness as a one-seventh power of the variable $(k_s/c)$ in the range from 4 X $10^{-7}$ to 5 X $10^{-4}$ from a more complicated expression. Hoerner [26] shows data of the minimum drag coefficients of smooth airfoils to be nearly constant for the Reynold's number from about 1 to 10 million, which is typical for general aviation at takeoff speeds. Since nocturnal frost generally will partially cover the wing section, it was desired to have a drag increment, $\Delta C_{D_c}$, instead of a drag coefficient so that as the fraction of frost coverage goes to zero, the drag increment will go to zero. It was found the drag increment approach has another advantage. From a cursory examination of Gregory and O'Reilly's [27], Clarius' [28], Ingelman-Sanberg's et al. [29], and Abbott and Von Doenhoff's [30] data concerning partially or fully roughened plain airfoil, it was found the drag difference penalty, $\Delta C_{D_c}$, tends to be a constant as a function of angle of attack until near the roughened airfoil stall angle. This assumption of constant drag difference would also make the corrections to the smooth airfoil drag coefficient due to roughness invariant to

aspect ratio effects or other drag components of the aircraft. Although the previous observations were for plain airfoils, they are assumed to apply also to the NACA 65A215 airfoil with 20° flaps partially covered by simulated frost. The empirical fit guided by the previous ideas to the Ljungstroem's data reproduced in Figure 11 for the drag coefficients resulted in the equation:

$$C_D = \Delta C_{D_C} + C_{D_C} \tag{A3.5}$$

where: $C_{D_C} = 0.0146 + 1.066 \times 10^{-4} (\alpha + 5.9)^2$, and, (A3.6)

$$\Delta C_{D_C} = [0.1344 (k_s/c)^{1/7} - 0.02595][1 - (1-P)^{1/2}]. \tag{A3.7}$$

It is recommended Equations (A3.5) to (A3.7) be used for the interpolation of the data. Equation (A3.7) was used in Table VIII to estimate the increment in the wing drag coefficient due to the wing surface roughness of the frost layer. The airfoil drag coefficient beyond the stall angle is given by [31] as:

$$C_D = 2.1 (\sin \alpha)^{1.7} \tag{A3.8}$$

In the nocturnal frost formation cases considered in this paper, the lift penalty has a severe effect on the climb performance. Brumby [3] correlated the relative maximum lift loss as a linear semi-log relationship to the variable $k_s/c$. But when the Reynold's number dependences are also considered, a lot of scatter was produced in the data versus $k_s/c$. When the relative maximum lift loss data by Brumby [3], Ljungstroem [2], Abbott and Von Doenhoff [30], and Gregory and O'Reilly [27] was replotted versus the variable $Re_c(k_s/c)$, on the semi-log scale, the scatter was significantly reduced. Only Ljungstroem data on the NACA 65A215 airfoil with 20° flaps and with or without 25° slats is shown here and is given by Figure 20. The open symbols data are without 25° slats and the solid symbols data are with the 25° slats. To include the effects of partial coverage of frost, P, a relationship similar to Equation (A3.4) was sought, but having a

semi-log relationship to the variable, $Re_c(k_s/c)$ resulted in the following empirical relationship as a fit to the open symbol data:

$$\frac{\Delta C_{L_m}}{C_{L_m}} = \left[.3016 + (.3880 - .3467P)\ln\left(\frac{Re(k_s/c)}{1093}\right)\right]\left[1 - (1-P)^{1/4}\right], \quad (A3.9)$$

as given by the solid lines in Figure 20. Equation (A3.9) should be understood for what it is, a reasonable empirical fit to the data on the relative maximum lift loss. There were not enough solid symbol data to establish any kind of empirical relationship for the 25° slats. Thus the dashed lines were simply drawn through the solid symbol data. In a slightly, but significantly, different manner than Brumby [3], the relative stall angle loss was simply correlated as:

$$\frac{\Delta \alpha_s}{\alpha_s} = C_0 \frac{\Delta C_{L_m}}{C_{L_m}} \quad (A3.10)$$

where the angle of attack is relative to the zero lift point. On the data reproduced from Ljungstroem in Figure 10 for the NACA 65A215 airfoil with 20° flaps, the value for $C_0$ was fitted as 0.725. To generate the curves in Figure 10 in the prediction of the lift coefficient as a function of angle of attack due to roughness, Equations (54) and (55) in the text, and the clean airfoil (instead of aircraft) lift curve was used. That is, take any point on the airfoil clean lift curve and reduce the lift coefficient value by Equation (54) and simultaneously also reduce the angle of attack value by Equation (55). Equations (A3.9) and (A3.10) were used in Table VIII and Equations (52) and (53) to estimate the relative lift loss, and the reduced angle of attack for takeoff.

# REFERENCES

1. Langston, P. A. S., "Hoar Frost on Aircraft Surfaces," Heathrow BEA-Engineering Tech. Note #P/570, Nov. 18, 1968.

2. Ljungstroem, Björn L. G., "Wind Tunnel Investigation of Simulated Hoar Frost on a 2 Dimensional Wing Section with and Without High Lift Devices," FFA-AU-902, April 1972.

3. Brumby, R. E., "Wing Surface Roughness - Cause & Effect," D.C. Flight Approach, No. 32, Jan 1979.

4. Weeks, D. J., "Tests on the Effect of Simulated Hoar Frost Deposits on the Take-off Performance of a Model of a Transport Aircraft (Hawker Siddeley Trident 3B)", RAE-TR-71178.

5. Dietenberger, M. A., "A Frost Formation Model and its Validation Under Various Experimental Conditions", UDR-TR-82-77.

6. Bagdonas, A., Georg, J. C., and Gerber, J. F., "Techniques of Frost Prediction and Methods of Frost and Cold Protection," WMO - No. 487.

7. Rohsenow & Hartnett, ed., Handbook of Heat Transfer, McGraw-Hill Book Company, 1973.

8. Threlkeld, J. L., ed., Thermal Environmental Engineering, Prentice-Hall, Inc., 1962.

9. Shampine, L. F., "Stiffness and Nonstiff Differential Equation Solvers II: Detecting Stiffness With Runge-Kutta Methods." ACM Trans on Mathematical Software, Vol. 3, No. 1, March, 1977; pages 44-53.

10. Jacobs, E. N. and Sherman, A., "Airfoil Section Characteristics As Affected by Variations of the Reynolds Number," NACA No. 586.

11. Biguria, B. and Wenzel, L. A., "Measurement and Correlation of Water Frost Thermal Conductivity and Density," I&EC Fundamentals, Vol. 9, No. 1, Feb 1970.

12. Frick, C. and McCullough, G., "A Method for Determining the Rate of Heat Transfer From a Wing or Streamline Body," NACA Report #830, pp. 627-636.

13. Bristov, D. R., "A New Surface Singularity Method for Multi-Element Airfoil Analysis and Design," AIAA 14th Aerospace Science Meeting, AIAA Paper No. 76-20, Jan 26-28, 1976.

14. Tajima, O., Yamada, H., Kobayoshi, Y., and Mizutani, C., "Frost Formation on Air Coolers. Part 1: National Convection for a Cooled Plate Facing Upward." Originally published in Refrigeration, 46, 333-341 (1971), translated by O. Tajima.

15. Churchill, S. W., "A Comprehensive Correlating Equation for Laminar, Assisting, Forced and Free Convection," AICHE Journal, Vol. 23, No. 1, Jan 1977, page 10.

16. Sparrow, E. M., Ramsey, O.W., and Mass, E. A., "Effect of Finite Width on Heat Transfer and Fluid Flow About an Inclined Rectangular Plate," ASME Journal of Heat Transfer, May 1979, Vol. 101, p. 199-204.

17. Grove, D., "User's Guide for Program NOCTFR (Nocturnal Frost/Ice Growth on an Airfoil), Contract No. NAS8-33369, Feb 1982.

18. Galins, P. and Shirkey M., "737 Wing Leading Edge Condition-Part II", Airliner, October 1977.

19. Fink, M.P., Freeman, D.C. and Greer, H.D., "Full-Scale Wind-Tunnel Investigation of the Static Longitudinal and Lateral Characteristics of a Light Single-Engine Airplane", NASA-TN-D-5700.

20. "Aircraft Accident Reports Brief Format U.S. Civil Aviation Issue Number 5 of 1977 Accidents" NTIS, U.S. Department of Commerce, Springfield, Virginia, 22151.

21. "NTSB Studies JAL Crash at Anchorage", Aviation Week and Space Technology, April 30, 1979, pp. 195-203.

22. "NTSB 737 Crash Conclusions Cite Passenger Rescue Efforts", Aviation Week and Space Technology, August 16, 1982, p. 30.

23. Irvine, W. M. and J. C. Pollock, "Infrared Optical Properties of Water and Ice Spheres", Icams 8, 1967, pp. 324-360.

24. McConnell, D., "Radiant Energy Transport Within Cryogenic Condensates", NASA Technical Memorandum X-52192, 1966. Also see Kislovskii. L.D., "Optics and Spectroscopy 7, 1959, pp. 201-206.

25. Young, F. L., "Experimental Investigation of the Effects of Surface Roughness of Compressible Turbulent Boundary Layer Skin Friction and Heat Transfer," DRL-532.

26. Hoerner, S. F. "Fluid-Dynamic Drag", Published by the Author, Check Membership Roster of AIAA.

27. Gregory, N., and O'Reilly, "Low Speed Aerodynamic Characteristics of NACA 0012 Aerofoil Section, Including the Effects of Upper-Surface Roughness Simulating Hoar Frost", ARC R&M #3726, 1973.

28. Clarius, U., "Ice Simulation - A 2-Dimensional Wind Tunnel Investigation of a NACA $65_2A215$ Wing Section with Single Slotted Flap," FFA-AU-995, part w, 1974.

29. Ingelman-Sandberg, M., Trunov, O. K., and Ivoniko, A., "Methods For Prediction of the Influence of Ice on Aircraft Flying Characteristics," Swedish-Soviet Working Group on Flight Safety - 6th Meeting, 1977, Report No. JR-1.

30. Abbott, I. H., Von Doenhoff, A. E., "Theory of Wing Sections", Dover Publications, Inc., N.Y., 1959.

31. Schwartzberg, M. A., "Airfoil Profile Drag," USAAVSCOM-TR-75-19.

| 1. REPORT NO. NASA CR-3733 | 2. GOVERNMENT ACCESSION NO. | 3. RECIPIENT'S CATALOG NO. | | |
|---|---|---|---|---|
| 4. TITLE AND SUBTITLE A Model for Nocturnal Frost Formation on a Wing Section - Aircraft Takeoff Performance Penalties | | 5. REPORT DATE October 1983 | | |
| | | 6. PERFORMING ORGANIZATION CODE | | |
| 7. AUTHOR(S) Mark A. Dietenberger | | 8. PERFORMING ORGANIZATION REPORT # | | |
| 9. PERFORMING ORGANIZATION NAME AND ADDRESS University of Dayton Research Institute Dayton, Ohio 45469 | | 10. WORK UNIT NO. M-422 | | |
| | | 11. CONTRACT OR GRANT NO. NAS8-33369 | | |
| | | 13. TYPE OF REPORT & PERIOD COVERED | | |
| 12. SPONSORING AGENCY NAME AND ADDRESS National Aeronautics and Space Administration Washington, DC 20546 | | Contractor Report | | |
| | | 14. SPONSORING AGENCY CODE | | |
| 15. SUPPLEMENTARY NOTES Marshall Space Flight Center, Systems Dynamics Laboratory, Atmospheric Sciences Division, Technical Monitor: Dennis Camp | | | | |

16. ABSTRACT

The research on the nocturnal frost formation on a wing section was undertaken to better explain the hazard associated with frost during takeoff. A model of nocturnal frost formation on a wing section has been developed that predicts when the nocturnal frost will form and also its thickness and density as a function of time. The model shows satisfactory comparison with the experimental data on a flat plate. An analysis of the aerodynamic penalties as related to the nocturnal frost formation properties was made to determine how much the takeoff performance would be degraded by a specific frost layer. With an aircraft takeoff assuming equations representing a steady climbing flight, it was determined a reduction in the maximum gross weight or a partial frost clearance and a reduction in the takeoff angle of attack are needed to neutralize drag and lift penalties due to frost. A sensitivity study was performed to determine the atmospheric conditions which produce the most hazardous frost buildup.

| 17. KEY WORDS Frost Icing Aircraft Icing Aircraft Safety | | 18. DISTRIBUTION STATEMENT Unclassified - Unlimited Subject Category 47 | | |
|---|---|---|---|---|
| 19. SECURITY CLASSIF. (of this report) Unclassified | 20. SECURITY CLASSIF. (of this page) Unclassified | | 21. NO. OF PAGES 94 | 22. PRICE A05 |